aerospace

MDPI

Article

Multi-Objective Manoeuvring Optimization for Multi-Satellite Responsive Earth Observation †

Annarita Argirò *, Nicola Cimmino, Giorgio Isoletta, Roberto Opromolla and Giancarmine Fasano

Department of Industrial Engineering, University of Naples Federico II, Piazzale Vincenzo Tecchio 80, 80125 Naples, Italy; nicola.cimmino@unina.it (N.C.); giorgio.isoletta@unina.it (G.I.); roberto.opromolla@unina.it (R.O.); g.fasano@unina.it (G.F.)

* Correspondence: annarita.argiro@unina.it

† This article is a revised and expanded version of our paper published in Optimized Multi-Satellite Manoeuvring Strategy for Responsive Earth Observation. In Proceedings of the Aerospace Europe Conference, Joint 10th EUCASS–9th CEAS Conference, Lausanne, Switzerland, 9–13 July 2023.

Abstract: Many space missions require that an area of interest on the ground is observed in a timely manner. Several approaches have been proposed in literature for this purpose, which involve modifying the ground track of an in-orbit satellite to overfly one or more Earth sites. Multi-satellite systems can clearly provide advantages for addressing this task in terms of responsiveness. In this context, this paper proposes a decision-making architecture to select the optimal manoeuvring or non-manoeuvring solution that enables a set of multiple sensor-equipped satellites in low Earth orbit to observe an area of interest in a timely fashion. For satellites that do not overfly the Earth site within the specified time period, dual coplanar impulsive manoeuvres are designed by applying a sensor-aware ground-track adjustment method. In particular, sensor footprints and percentage coverage of the assumed areas of interest are explicitly taken into account. A multi-objective optimization problem is then solved to determine which satellite provides the best solution to cover the area of interest in terms of fuel consumption (if ground-track adjustment is required) and time to overflight. Both simulated and real-world scenarios are considered to numerically validate the proposed methodology.

Keywords: responsive space; ground-track adjustment; sensor-aware coverage analysis; multi-objective optimization

check for updates

Academic Editors: Pierre Rochus, M. Reza Emami, Shuang Li and Hongwei Yang

Received: 9 January 2025
Revised: 5 February 2025
Accepted: 9 February 2025
Published: 13 February 2025

Citation: Argirò, A.; Cimmino, N.; Isoletta, G.; Opromolla, R.; Fasano, G. Multi-Objective Manoeuvring Optimization for Multi-Satellite Responsive Earth Observation. *Aerospace* **2025**, *12*, 143. https://doi.org/10.3390/aerospace12020143

Copyright: © 2025 by the authors. Licensee MDPI, Basel, Switzerland. This article is an open access article distributed under the terms and conditions of the Creative Commons Attribution (CC BY) license (https://creativecommons.org/licenses/by/4.0/).

1. Introduction

In recent years, the capability to respond to real-time events by providing data on-demand for time-critical tasks has become paramount, especially for monitoring or search and rescue operations during natural disasters like earthquakes, forest fires, and floods [1,2]. To enhance space responsiveness, two different strategies can be adopted. On the one hand, miniaturization and standardization of space systems can be exploited to enable responsive launch capabilities, after solving an optimal orbit design problem [3–5]. On the other hand, orbital and/or attitude manoeuvres can be commanded to adjust the ground tracks and/or the observable areas of in-orbit satellites, thus achieving fast Earth observation for specified ground targets [6]. The latter approach, referred to as the ground-track adjustment, has attracted increasing interest in the last few years.

The ground-track adjustment problem has been addressed in the current literature by using either impulsive manoeuvres (provided by chemical propulsion systems) or low-thrust manoeuvres (based on electric propulsion systems). Co et al. [7] presented a method

to quantify the terrestrial distance between the sub-satellite points of a non-manoeuvring satellite in a reference orbit and a manoeuvring one using chemical or electric propulsion for a given propellant budget, initial orbit, and available manoeuvring time. In order to design a suitable initial orbit, they also investigated how the changes in orbital elements influence the ground track, and they found that altitude and eccentricity have the greatest effects [7]. Zhang and Cao [8] derived a single-impulse method to reach a free (i.e., with no constraints) elliptical final orbit and a shape-based low-thrust method to obtain an assigned final orbit (e.g., repeated ground-track orbit or sun-synchronous orbit) to solve the coplanar ground-track adjustment problem. For the single-impulse method, they obtained the semi-major axis of the final orbit by solving a cubic equation. For the continuous low-thrust case, instead, the desired trajectory is modelled as a specified-form shape function with coefficients obtained from boundary conditions. Both methods are based on the time difference for the two-body model, to avoid dealing with the J_2 perturbation, which is only considered when computing the longitude difference [8]. For the cases in which impulsive propulsion is available, Zhang et al. [9] proposed a one- and two-impulse approach to reach an elliptical and a circular free final orbit, respectively. In particular, approximate analytical solutions are derived by solving analytically the semi-major axis of the final orbit, accounting for the linear J_2 perturbation, considering the possibility of either reaching an exact overflight on a ground target or keeping it with a conical sensor field of view. In contrast to the impulsive approaches suggested in Refs. [8,9], which achieve free final orbits whose ground track passes over the Earth site, Zhang and Sheng [10] addressed the impulsive coplanar ground-track adjustment problem to obtain an assigned final orbit. Specifically, they introduced three-impulse and four-impulse methods for coplanar circular and noncoaxial elliptical orbits, respectively. Recently, Sheng and Geng [2] provided an analytical approach based on the normalized nodal distance to solve the J_2-perturbed ground-track adjustment problem under apsidal-altitude constraints using a single impulse.

The above-mentioned ground-track adjustment methods focused on finding manoeuvring solutions for observing one target. However, the ground track can also be adjusted to observe multiple Earth sites. For the low-thrust manoeuvre case, Co and Black [11] developed a control algorithm for a single low Earth orbit (LEO) satellite equipped with an electric propulsion system to pass over 10 randomly selected ground targets. Guelman and Shiryaev [12] introduced a closed-loop control algorithm that allows the direct flyover of the selected Earth sites without the need for precomputed reference trajectories. For the impulsive manoeuvre case, Mok and Bang [13] proposed near-optimal solutions for overflying one, two, and three ground targets. For this purpose, they considered at least one manoeuvre to observe each target. Conversely, Lin et al. [6] used a single coplanar impulse to solve the ground-track adjustment problem for overflying one to three ground targets at most.

Nowadays, the ground-track adjustment approach becomes particularly appealing for space actors (i.e., space agencies, industries, and private stakeholders) which can rely on more than one satellite to manoeuvre. Indeed, the possibility of relying on multi-satellite systems helps in optimizing the trade-off between propellant expense and responsive observation requirements. In this context, Yu et al. [14] suggested two constellation design approaches based on the reachable domain belts of a single satellite. Reachable domain belts are generated by making use of the ground-track shift due to the period difference between a reference orbit and a manoeuvred one. Two- and one-impulse manoeuvres are considered for this purpose. Other works, on the other hand, dealt with the reconfiguration of a constellation of multiple satellites. De Weck et al. [15] used the auction algorithm to determine how to best assign each satellite of an existing constellation to a spot in a new constellation such that the fuel consumption required for the reconfiguration is

minimized. McGrath and Macdonald [16] considered a constellation of 24 satellites in four orbital planes to be manoeuvred into repeating ground-track orbits, and introduced a simple utility function to decide which satellite should be manoeuvred during each reconfiguration. Their work demonstrated that reconfiguring a constellation of satellites can provide increased coverage of 1.6–10 times compared to a static, global-coverage constellation. Kandepi et al. [17] proposed an efficient heuristic approach for the scheduling problem for imaging a large area target using a constellation of multiple satellites. Other works suggest different approaches for scheduling operations of multiple agile satellites to overfly multiple targets [18]. In particular, Zhang et al. [19] presented a multitree search framework for the multi-satellite responsiveness scheduling problem considering orbital impulsive manoeuvring. Zhang et al. [20] also proposed a multi-trajectory combination framework to optimize the observation sequence and design the trajectory of the satellite. Du et al. [21] provided a data-driven parallel scheduling approach to predict the probability that a task will be fulfilled by different satellites. Luo et al. [22] addressed the orbit manoeuvre optimization problem by proposing three models that aim to optimize response time, ground resolution, and fuel consumption to satisfy diverse user requirements. Yin et al. [23], instead, focused on solving the multiple-satellite orbit manoeuvre optimization problem by developing a multi-objective optimization model that considers response time, ground resolution, and fuel consumption as evaluation criteria. In Ref. [24], Artificial Intelligence is adopted to facilitate a more responsive and resilient approach to Space-Based Space Surveillance, improving autonomous planning and reconfiguration capabilities.

Given this framework, this paper proposes an original decision-making architecture for a responsive multi-satellite system in LEO. The architecture outputs an optimal solution to overfly a user-specified Earth site within an assigned time frame considering both manoeuvring and non-manoeuvring options. Within the architecture, a sensor-aware fine ground-track adjustment method, building upon the analytical method proposed by Zhang et al. [9], has been integrated in a multi-objective optimization framework. The main innovative points of the proposed methodology are listed below.

- Unlike works dealing with the ground-track adjustment problem, which consider only optical payloads with a conical field of view, the proposed sensor-aware ground-track adjustment method accounts for the availability of different types of remote sensing sensors, i.e., either optical cameras or radars, by considering a pyramidal-shaped field of view. Furthermore, differently from other state-of-the-art works, the proposed methodology does not define the Earth site as a point target, but as an area of interest (AOI) characterized by a range of latitudes and longitudes. The introduction of ad hoc metrics to assess the quality of the overflight is required when considering an extended target instead of a point target. A particularly relevant metric for evaluating the overflight of an AOI is the coverage percentage. Therefore, in this work, overflight conditions are assessed based on a minimum requirement in terms of AOI coverage percentage.
- Once all feasible options are identified, a multi-objective optimization problem is formulated weighting both fuel consumption and time responsiveness constraints. Unlike state-of-the-art works, after determining the set of equally optimal solutions, a decision-making method is applied to select the optimal solution according to the decision-making preferences.
- This algorithm is fully scalable and adaptive with respect to the characteristics of the satellites and payloads and, thus, can be applied to different satellite groups. Differently from state-of-the-art works [25], the algorithm does not require hypotheses on the relative geometry between the satellites (as for satellite constellations). Moreover, being based on short-period numerical propagation, analytical manoeuvre design, and

non-combinatorial optimization, it requires a low computational cost and, therefore, it can be used on quasi-real time applications, such as emergency scenarios.

- Beyond optimizing the trade-off between propellant consumption and response time, the proposed approach also reduces the age of information (AoI), a metric that quantifies the timeliness of received data by measuring the time elapsed since the last update. By ensuring the timely overflight of AOI, the system facilitates the acquisition of up-to-date data, limiting the need for post-processing and improving operational effectiveness in critical situations.

Moreover, it is assumed that all the candidate Earth observation satellites possess adequate on-board propellant resources to carry out responsive manoeuvring if asked for (for instance, in a disaster-monitoring scenario).

Initial results corresponding to a preliminary implementation of this method can be found in [26]. Compared to [26], this paper introduces an assessment of the overflight conditions to ensure that the optimal manoeuvring or non-manoeuvring solution provided by the decision-making architecture meets a minimum requirement in terms of coverage percentage of the AOI. Therefore, this paper presents the consolidated design strategy and provides a complete assessment of its performance. Specifically, a numerical analysis on simulated test cases is carried out to show the effect on performance of variability in the type of on-board sensors, in the area of interest, and in the number of available satellites. Finally, the architecture is also tested considering a simulated scenario involving a set of real Earth observation satellites.

The remainder of the paper is organized as follows. Section 2 introduces the proposed decision-making architecture, describing the ground-track adjustment methodology and the multi-objective optimization. Section 3 presents the selected test cases and the results obtained. Section 4 draws some conclusions and discusses potential future works.

2. Multi-Satellite Responsive Manoeuvring Architecture

A flow diagram of the decision-making architecture for multi-satellite responsive manoeuvring is shown in Figure 1.

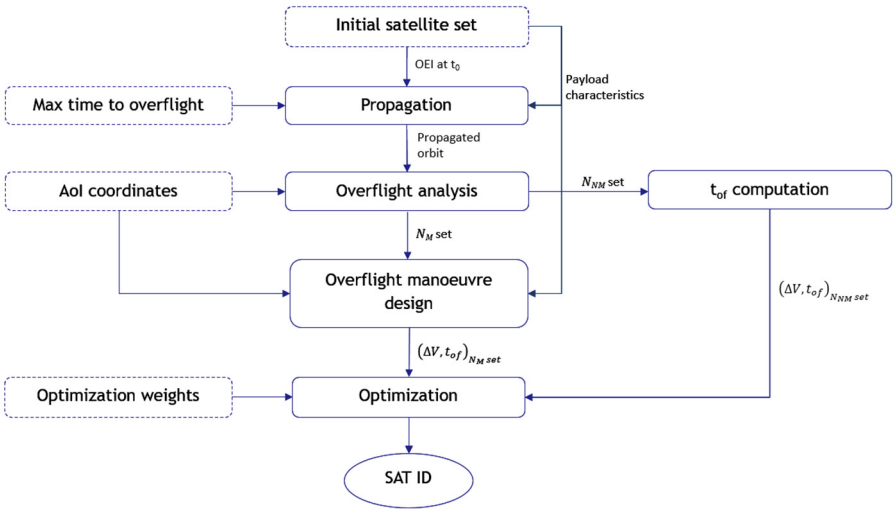


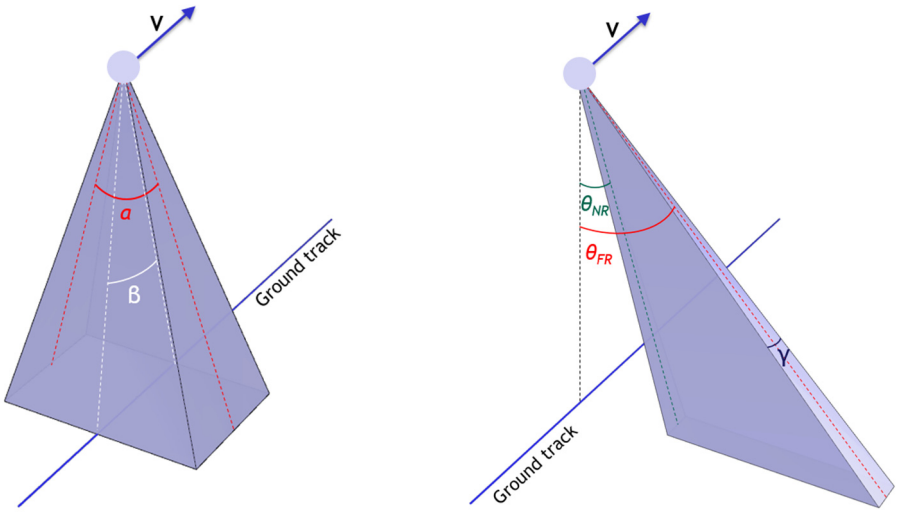
Figure 1. Flow diagram of the decision-making architecture for multi-satellite responsive manoeuvring.

This architecture requires the inputs listed below.

1. A set of N_{sat} satellites, each identified by its orbital parameters (OEI_{0i}) at an initial epoch t_0 and by its physical features (i.e., mass, m, area exposed to the drag, A_{drag}, and drag coefficient, C_d). In addition, each satellite is assumed to be equipped with

either an optical or a radar Earth-observation sensor modelled by a pyramidal-shaped field of view (FOV). The optical sensor is assumed to be nadir pointing, and its FOV is described by the angular size in the cross-track (α) and tangential (β) directions; the radar sensor FOV is instead defined by the minimum, θ_{min}, and maximum, θ_{max}, off-nadir angles, as well as the in-track angle, γ. This latter angle is functional to the overflight analysis for the sake of sensor FOV modelling and it should be consistent with orbit dynamics and sampling. It is not necessarily linked to a physical parameter of the considered radar since Synthetic Aperture Radar operation works by observing a lateral strip, integrating data in a multi-temporal fashion. A graphical representation of the sensors' FOV modelling is provided in Figure 2.

2. An Earth site, i.e., the target area of interest. This area is defined as a polygon, whose vertexes are assigned in terms of geodetic coordinates, namely latitude, ϕ, and longitude, λ.
3. The maximum admissible time to overflight, D, expressed as an integer number of days.
4. The weights for the optimization algorithm that measure the relative importance between the constraints on propellant consumption (expressed in the form of the total ΔV required for the responsive manoeuvre) and on the time to overflight, t_{of}. The definition and rationale for selection of these weights is addressed in Section 2.2.



(**a**) (**b**)

Figure 2. Graphical representation of the optical (**a**) and radar (**b**) sensor field of view and ground swath.

In the propagation block, the trajectories of the N_{sat} satellites are propagated for D days starting from t_0 to check whether an overflight would occur within the given time constraint without the need for manoeuvring. The propagation is performed by using NASA's General Mission Analysis Tool (GMAT), including the J_2 effect and drag, which are the most important perturbations in LEO.

The resulting ephemerides, the AOI coordinates, and the remote sensing payload's specifications are used as input for the overflight analysis block, which is applied to each satellite, according to the following steps. First, the footprint, i.e., the projection of the sensor FOV on the Earth surface, must be computed. To this aim, the FOV is modelled as the solid angle identified by a rectangular pyramid with the apex in the satellite position (assuming a nadir pointing and an off-nadir pointing for the optical and radar sensor, respectively). At each time instant of the ephemerides, the ground points delimiting the

footprint are computed in geodetic coordinates as the intersections between the vertices of the pyramidal FOV and the spherical Earth. It should be highlighted that the footprint has four vertices when dealing with a pyramid-shaped FOV. On the other hand, the case of the cone-shaped FOV can easily be treated by approximating the circular footprint with a 60-vertex polygon. At this point, the overflight analysis is required to verify the existence of an overlap between the resulting footprint and the AOI. To avoid carrying out this analysis for each time instant of the ephemeris and thus to improve computational efficiency, all the instances at which the AOI observation is not possible (e.g., the satellite is overflying the anti-meridian of the AOI) must be discarded. To this aim, a safe area is introduced, which is defined as the rectangle that includes the initial AOI with increased dimensions, given by the maximum variations of longitude and latitude between two consecutive time instants in the reference ephemerides, as shown in Figure 3. Consequently, only the time instances at which at least one vertex of the footprint falls within the safe area are considered for the subsequent step of the overflight analysis. Specifically, the resulting time intervals are sampled with an ad hoc time step (at least one order of magnitude smaller than the time step of the ephemerides) to interpolate the position and velocity vectors of the ephemerides. At each of these refined time steps, the sensor's footprint is evaluated to check whether at least one of the vertices of the footprint falls within the AOI or alternatively whether the sides of the footprint polygon intersect the sides of the AOI polygon. The first- and last-time instants at which either condition occurs represent the overflight start and end conditions, respectively.

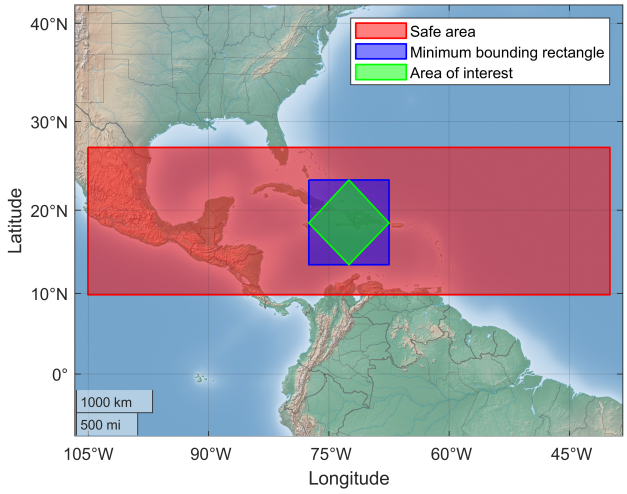


Figure 3. Example of area of interest (in green) from which the minimum bounding rectangle (in blue) and the resulting safe area (in red) are defined.

The overflight analysis block outputs a subset of satellites passing over the AOI within the required time without the need for manoeuvring, and their corresponding time to overflight (t_{of}). The number of such satellites is indicated as N_{NM}, which can go from 0 to N_{sat} in the most general case. The remaining satellites (whose number, N_M, is equal to $N_{sat} - N_{NM}$) are input to the overflight manoeuvre design block, which implements the ground-track adjustment method from [9], customized to account for the effective size of the optical and radar sensor swath width. The operations conducted in this block, which are described in detail in Section 2.1, output the required impulsive ΔV and the t_{of} for each of the N_M satellites.

Finally, such solutions in terms of ΔV and t_{of} are input to the optimization block, which implements the multi-objective optimization strategy described in detail in Section 2.2 to identify the most convenient solution to collect data from the AOI. Therefore, the proposed

architecture outputs the ID of the satellite that is most suitable for manoeuvring, according to the weights assigned by the decision-making preferences.

2.1. Ground-Track Adjustment Methodology

This section describes the approximate analytical method derived by Zhang et al. [9] (see Section 2.1.1) and how it is customized to account for the coverage of remote sensing sensors installed on board Earth observation satellites with pyramidal-shaped FOVs (see Section 2.1.2).

2.1.1. Fundamentals of the Ground-Track Adjustment Method

Given a site of interest on ground (P_S), identified by its geodetic latitude (λ_S) and longitude (ϕ_s), and a satellite on an initial circular or elliptical orbit, the method allows for defining a dual coplanar impulsive manoeuvre, producing a transfer to a final circular orbit which passes over the site itself. The method's approximation stems from considering the Earth oblateness (by means of the J_2 term of the gravitational potential) while discarding the perturbations due to drag, third bodies, solar radiation pressure, and higher order gravitational terms. The overflight condition is determined by the passage of the satellite's ground track on the Earth site.

In the case of a satellite on a circular orbit, a first solution must be obtained under the Keplerian motion assumption. The Keplerian time to overflight ($t_{of,k}$) can be obtained exploiting the Greenwich mean sidereal time (GMST) variation through Equation (1),

$$t_{of,k} = \frac{(\alpha_{Gt} - \alpha_{G0}) + 2\pi(D-1)}{\omega_\oplus} \tag{1}$$

where $\omega_\oplus = 7.2921158553 \times 10^{-5}$ rad/s is the Earth rotation rate (assumed to be constant), D is still the maximum time to the expected overflight, α_{Gt} and α_{G0} are the GMST angles when the sub-satellite point is P_S and at the initial time, respectively. The same quantity can also be computed using Equation (2), which derives from the assumption of using a Hohmann transfer to reach the target orbit.

$$t_{of,k} = \pi\sqrt{\frac{(a_0 - a_{S,k})^3}{8\mu}} + (u_t - u_{00} - \pi + 2\pi N_R)\sqrt{\frac{{a_{S,k}}^3}{\mu}} \tag{2}$$

The first term in Equation (2) is the transfer time for the Hohmann-transfer arc (t_H), which depends on the semi-major axis of the initial orbit (a_0), the unknown semi-major axis of the final orbit under the Keplerian motion assumption ($a_{S,k}$), and the Earth gravitational parameter (μ). Concerning the other terms, u_{00} is the argument of latitude of the satellite on the initial orbit at the initial time, u_t is the argument of latitude of the satellite on the final orbit when passing over P_S, and N_R is the number of orbit revolutions that minimize the required ΔV. In particular, u_t and N_R are computed according to Equation (3),

$$\begin{aligned} u_t &= \sin^{-1}\left(\frac{\sin\varphi_s}{\sin i_0}\right) \\ N_R &= \frac{1}{2\pi}\left(t_{of,k}\sqrt{\frac{\mu}{a_0^3(1+e_0)^3}} - u_t + u_{00}\right) \end{aligned} \tag{3}$$

where i_0 is the inclination of the initial orbit and e_0 is the eccentricity of the initial orbit (which is equal to 0 in the case of the initial circular orbit).

Given the equivalence between Equations (1) and (2), and since $t_{of,k}$ can be computed from Equation (1), $a_{S,k}$ can be derived solving Equation (4).

$$\left[\frac{\pi}{4} + (u_t - u_{00} - \pi + 2\pi N_R)\right]\left(\sqrt{a_{S,k}}\right)^3 + \frac{3\pi}{4}a_0\sqrt{a_{S,k}} - t_{of,k}\sqrt{\mu} = 0 \tag{4}$$

The J_2 effect cannot be neglected when the time of flight is of the order of several days. Under the linear J_2 perturbation, the semi-major axis (a), the eccentricity (e), and inclination (i) remain constant, while the argument of perigee (ω), the right ascension of the ascending node (Ω), and the mean anomaly (M) change according to Equation (5),

$$\begin{gathered}\dot{\omega}_{J_2} = C_{J_2}\left(2 - \tfrac{5}{2}\sin^2 i\right)/\left(1 - e^2\right)^2 \\ \dot{\Omega}_{J_2} = -C_{J_2}\cos i/\left(1 - e^2\right)^2 \\ \dot{M}_{J_2} = C_{J_2}\left(1 - \tfrac{3}{2}\sin^2 i\right)/\left(1 - e^2\right)^{3/2}\end{gathered} \tag{5}$$

where $C_{J_2} = 1.5\ J_2\ R_\oplus^2\sqrt{\mu}a^{-7/2}$ and $J_2 = 1.082627 \times 10^{-3}$.

The value of t_{of} under the J_2 effect can thus be obtained using the GMST variation through Equation (6), as well as by means of the approximate expression (7).

$$t_{of} = \frac{\alpha_{Gt} - \alpha_{G0} + 2\pi(D-1)}{\omega_\oplus - \dot{\Omega}_{J_2}} \tag{6}$$

$$t_{of} \approx \chi_{H_s}\pi\sqrt{\frac{(a_0 + \overline{a})^3}{8\mu}} + \chi_s(u_t - u_{00} - \pi + 2\pi N_R)\sqrt{\frac{\overline{a}^3}{\mu}} \tag{7}$$

In Equation (7), $\overline{a}$ is the unknown mean semi-major axis of the final orbit while χ_{H_s} and χ_s are correction factors, which can be computed through Equation (8).

$$\chi \triangleq \left[1 + \left(\dot{M}_{J_2} + \dot{\omega}_{J_2}\right)\sqrt{\overline{a}^3/\mu}\right]^{-1} \tag{8}$$

Specifically, χ_s and χ_{H_s} are obtained by replacing a and e in Equation (5) with $a_{s,k}$ and $e_0 = 0$ and with $a_H = (a_{s,k} + a_0)/2$ and $e_H = \left|a_{s,k} - a_0\right|/(a_{s,k} - a_0)$, respectively.

The equivalence between Equations (6) and (7) leads to a cubic equation in terms of $\sqrt{\overline{a}}$, which can be used to obtain the mean semi-major axis of the final orbit under the J_2 effect.

$$\left[\frac{\pi}{4}\chi_{H_s} + \chi_s(u_t - u_{00} - \pi + 2\pi N_R)\right]\left(\sqrt{\overline{a}}\right)^3 + \frac{3\pi}{4}\chi_{H_s}a_0\sqrt{\overline{a}} - t_{GJ_2}\sqrt{\mu} = 0 \tag{9}$$

The other orbital elements of the final orbit are identical to those of the initial orbit: they are first set as mean orbital elements and then transformed into osculating ones. The osculating semi-major axis of the final orbit (a_f) is finally used to determine the ΔV_{tot} required by the manoeuvring satellites considering a two-impulse Hohmann-transfer manoeuvre, as expressed by Equation (10).

$$\Delta V_{tot} = \sqrt{\frac{\mu}{a_0}}\left|\sqrt{\frac{2a_f}{a_0 + a_f}} - 1\right| + \sqrt{\frac{\mu}{a_f}}\left|1 - \sqrt{\frac{2a_0}{a_0 + a_f}}\right| \tag{10}$$

The first impulse is applied at the initial time, while the second impulse is applied at the apogee of the transfer orbit, whose time instant is given by the first term at the right-hand side of Equation (7).

When starting from the initial elliptical orbit, on the other hand, $t_{of,k}$ is computed using Equation (11),

$$t_{of,k} = (\pi - M_{00})\sqrt{\frac{a_0^3}{\mu}} + \pi\sqrt{\frac{[a_0(1+e_0)+a_{s,k}]^3}{8\mu}} + (u_t - \omega_0 + 2\pi N_R)\sqrt{\frac{{a_{s,k}}^3}{\mu}} \quad (11)$$

where e_0 is the eccentricity of the initial orbit, M_{00} is the mean anomaly of the initial orbit at the initial time, and ω_0 is the argument of perigee of the initial orbit. In Equation (11), the first term stands for the coasting time $t_{coasting}$ required to reach the apogee of the initial orbit and the second term stands for the Hohmann-transfer time t_H. As in the previous case, the Keplerian semi-major axis of the final orbit, $a_{s,k}$, is first obtained by solving Equation (12), which derives from the equivalence between Equations (11) and (1).

$$\left[\frac{\pi}{4} + (u_t - \omega_0 + 2\pi N_r)\right](\sqrt{a_{s,k}})^3 + \frac{3\pi}{4}a_0(1+e_0)\sqrt{a_{s,k}} - \left[t_{of,k}\sqrt{\mu} - (\pi - M_{00})\right]\sqrt{a_0^3} = 0 \quad (12)$$

The value of $a_{s,k}$ is used to determine $\dot{\omega}_{J_2}$, $\dot{\Omega}_{J_2}$, and $\dot{M}_{J_2}$ through Equation (5), while $t_{of,k}$ is calculated through Equation (1). As in the case of initial circular orbit, a value of t_{of}, which accounts for the J_2 effect, can be computed using Equation (13).

$$t_{of} \approx t_{coasting} + \chi_{H_s}\pi\sqrt{\frac{[a_0(1+e_0)+\bar{a}]^3}{8\mu}} + \chi_s(u_t - \omega_0 + 2\pi N_R)\sqrt{\frac{\bar{a}^3}{\mu}} \quad (13)$$

In Equation (13), $t_{coasting}$ is obtained using numerical propagation (in our case, Runge–Kutta 89 is used as the integrator), while the parameters χ_s and χ_{H_s} are given by Equation (8). Specifically, χ_s and χ_{H_s} are obtained by replacing a and e in Equation (5) with $a_{s,k}$ and e_0 and with $a_{H_s} = [a_{s,k} + a_0(1+e_0)]/2$ and $e_{H_s} = [a_{s,k} - a_0(1+e_0)]/[a_{s,k} + a_0(1+e_0)]$, respectively.

Given the equivalence between Equations (13) and (6), a cubic equation in terms of $\sqrt{\bar{a}}$ can be again formulated, whose solution allows the computation of the desired mean semi-major axis of the final orbit.

$$\left[\frac{\pi}{4}\chi_{H_s} + \chi_s(u_t - \omega_0 + 2\pi N_R)\right]\left(\sqrt{\bar{a}}\right)^3 + \frac{3\pi}{4}\chi_{H_s}a_0(1+e_0)\sqrt{\bar{a}} - \left(t_{of} - t_{coasting}\right)\sqrt{\mu} = 0 \quad (14)$$

The other orbital elements of the final orbit are identical to those of the initial orbit at $t_{coasting}$. These orbital parameters are set as mean orbital elements and then they are transformed into osculating ones. Again, the osculating semi-major axis, a_f, is used to determine the value of ΔV_{tot}, considering a Hohmann-transfer manoeuvre and applying the first impulse at the apogee, through Equation (15).

$$\Delta V_{tot} = \sqrt{\frac{\mu}{a_0(1+e_0)}}\left|\sqrt{\frac{2a_f}{a_0(1+e_0)+a_f}} - \sqrt{1-e_0}\right| + \sqrt{\frac{\mu}{a_f}}\left|1 - \sqrt{\frac{2a_0(1+e_0)}{a_0(1+e_0)+a_f}}\right| \quad (15)$$

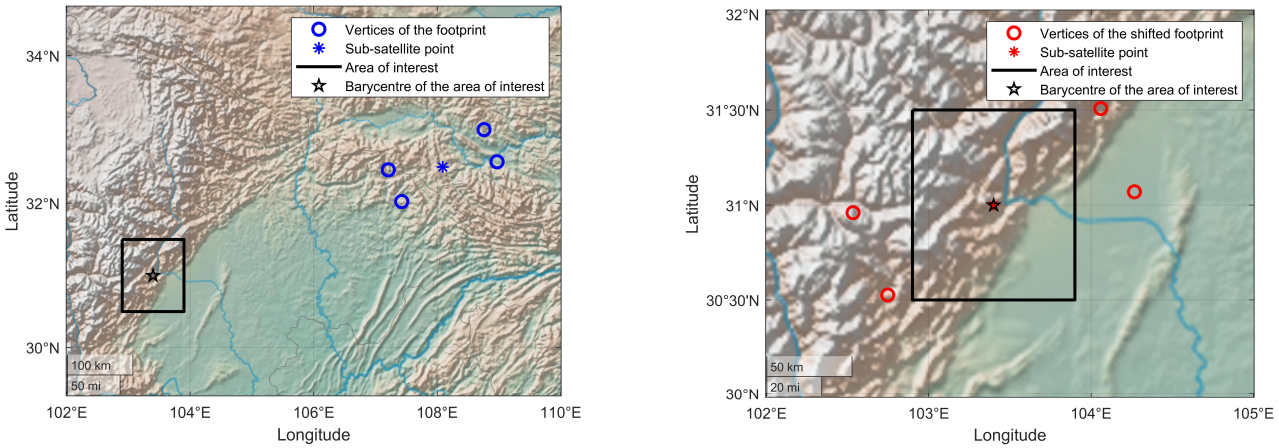
The first impulse is applied at the apogee of the initial orbit, i.e., at $t_1 = t_{coasting}$, while the second impulse occurs at the apogee of the transfer orbit, i.e., at $t_2 = t_{coasting} + t_H$.

2.1.2. Sensor-Aware Correction Approach

The analytical method, presented by Zhang et al. in [9] and briefly recalled in Section 2.1.1, leads to an approximate solution and a residual distance between the target and the sub-satellite point of a few kilometres. Such a distance might not be representative of the actual observability of the AOI from a sensor-equipped satellite, as the target might not be within the sensor footprint. For this reason, in the same work, the analytical solutions are also extended to the case of a satellite equipped with a nadir-pointing conical sensor.

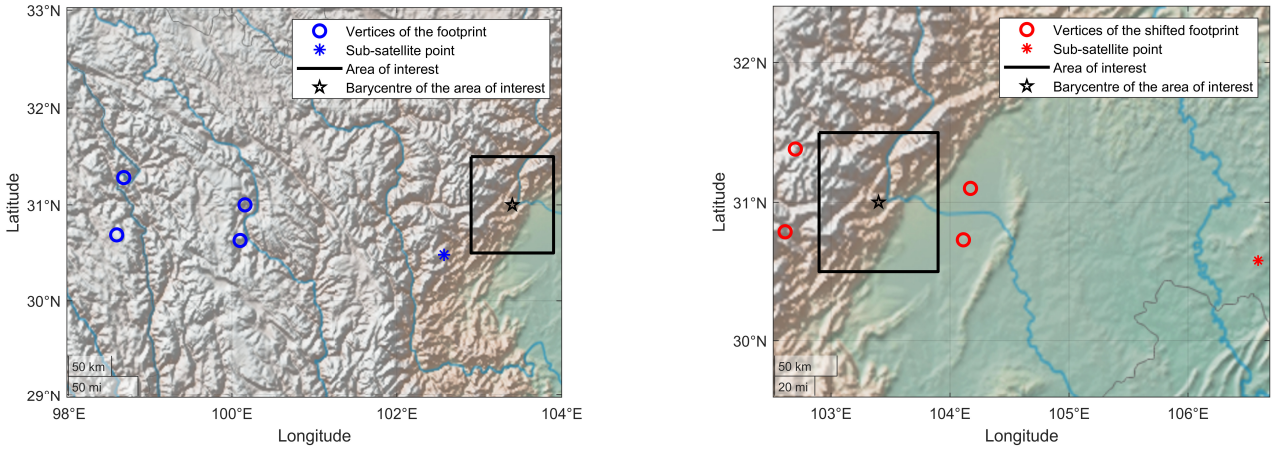
To accomplish that, they applied the analytical method so that the target is located at the boundary of the conical sensor footprint, resulting in a reduction in fuel consumption. In this paper, the two-impulse method derived by Zhang et al. [9] is modified assuming that the satellite is equipped with either a nadir pointing optical sensor or an off-nadir pointing radar, both with a pyramidal-shaped FOV. To be conservative, the analytical method is applied so that the target is placed at the centre of the optical sensor or radar footprint.

The following procedure is applied to all the N_M satellites, as identified by the overflight analysis block of the proposed architecture (see Figure 1). For these satellites, at each time instant of their orbit ephemerides, there is no intersection between the AOI, whose centre coordinates are indicated as $P_{AOI}(\lambda_{AOI}, \phi_{AOI})$, and the footprint, whose centre coordinates are indicated as $P_{FP}(\lambda_{FP}, \phi_{FP})$. Examples are shown in Figure 4a and in Figure 5a.



(**a**) (**b**)

Figure 4. Example of unsuccessful overflight by the satellite's optical sensor (**a**) and successful overflight by the satellite's optical sensor (**b**). The footprint of the optical sensor is shown in blue: the empty dots are the vertices of the footprint, and the asterisk is the sub-satellite point. Black lines mark the area of interest, and the black star represents the barycentre of the area of interest. The shifted footprint of the optical sensor is depicted in red.



(**a**) (**b**)

Figure 5. Example of unsuccessful overflight by the satellite's radar (**a**) and successful overflight by the satellite's radar (**b**). The footprint of the radar is shown in blue: the empty dots are the vertices of the footprint, and the asterisk is the sub-satellite point. Black lines mark the area of interest, and the black star represents the barycentre of the area of interest. The shifted footprint of the radar is depicted in red.

In the case of an optical satellite, given the nadir pointing assumption, the sub-satellite point $P_{SSP}(\lambda_{SSP}, \phi_{SSP})$ coincides with P_{FP}. Thus, the ground-track adjustment problem described in the previous subsection is solved by setting $P_{AOI} \equiv P_{SSP} \equiv P_{FP}$ as the Earth site. This condition should lead to an overflight, as shown in Figure 4b, aside from residual errors due to the inherent approximations of the method in [9].

In the case of a radar-equipped satellite, given the off-nadir pointing assumption, the ground-track adjustment problem described in the previous subsection must be solved by setting as the Earth site the P_{SSP} at which $P_{FP} \equiv P_{AOI}$. To this aim, the ground distance ($d_{SPP,FP}$) between P_{SSP} and P_{FP} on the surface of the Earth modelled as an ellipsoid, whose semi-major axis is 6378.137 km and whose eccentricity is 0.0818, is calculated according to [27]. It is also required to compute the off-nadir angle of P_{FP} with respect to P_{SSP} (ϑ_{FP}) using the Equation (16). Please note that the inverse tangent function in (16) is the two-argument arctangent.

$$\theta_{FP} = tan^{-1}\left(\frac{\sin(\lambda_{SSP} - \lambda_{FP})\cos(\phi_{SSP})}{\cos(\phi_{FP})\sin(\phi_{SSP}) - \sin(\phi_{FP})\cos(\phi_{SSP})\cos(\lambda_{SSP} - \lambda_{FP})}\right) \tag{16}$$

Finally, the geodetic coordinates of the desired P_{SSP} can be computed using Equation (17),

$$\begin{aligned} \phi_{SSP} &= \phi_{AOI} + \frac{d_{SSP,FP}}{R}\cos(\theta_{FP}) \\ \lambda_{SSP} &= \lambda_{AOI} + \frac{d_{SSP,FP}}{R}\sin(\theta_{FP})\frac{1}{\cos(\phi_{FP})} \end{aligned} \tag{17}$$

where R is the Earth radius.

For satellites equipped with an optical sensor, illumination conditions are taken into account with a simplified strategy and, thus, only overflight solutions that occur during the daytime are considered. To discriminate between day and night, dawn and dusk are computed using standard astronomical algorithms [28] and considering civil dawn and dusk (i.e., the sun at 6° below the horizon) as the criterion for the start and end of the daylight period.

Besides disregarding overflights that take place under insufficient illumination conditions for satellites equipped with an optical sensor, solutions that do not enable us to achieve a minimum coverage percentage, assumed to be 30%, are also eliminated. To this end, the coverage percentage is evaluated as the ratio between the area overflown by the satellite and the total area of interest. Denoting as x and y the Cartesian coordinates obtained by projecting the latitude and longitude coordinates of the N vertices of the area of interest, considering the Universal Transfer Mercator (UTM) projection, the total area is computed using the Shoelace formula [29], given in (18).

$$A = \frac{1}{2}\left|\sum_{i=1}^{N-1}(x_i y_{i+1} - y_i x_{i+1}) + (x_N y_1 - y_N x_1)\right| \tag{18}$$

The area overflown by the satellite is obtained as the result of the intersection between the AOI and the polygon obtained from the union of all the footprints of the sensor entering the AOI, as shown in Figure 6. Specifically, the intersection area between the two polygons is computed by first identifying intersecting edges using geometric algorithms. Then, each polygon is cut out using the edges of the other, retaining the vertices that define the overlapping region. From these vertices, the intersecting polygon is constructed, and its area is calculated using (18).

Regarding the manoeuvring satellites, it is assumed that all the candidates possess adequate on-board propellant resources to carry out responsive manoeuvring if asked for (for instance, in a disaster-monitoring scenario).

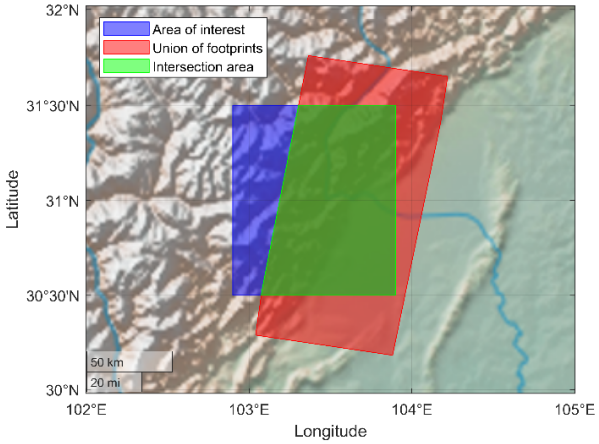


Figure 6. Example of intersection area (in green) between the polygon obtained as a result of the union of the footprints that overfly the area of interest in red and the area of interest in blue.

2.2. Multi-Objective Optimal Ground-Track Adjustment

Multi-objective optimization is applied in many real-world engineering problems where objectives under consideration conflict with each other, and optimizing a particular solution with respect to a single objective can result in unacceptable results with respect to the other objectives [30]. Multi-objective optimization problems provide a set of equally optimal solutions, referred to as Pareto-optimal solutions or non-dominated solutions, which form the Pareto optimal front. A solution is said to be non-dominated if it cannot be improved with respect to any objective without worsening at least one other objective. In contrast, dominated solutions are those for which at least one non-dominated solution that maximizes/minimizes all the objectives exists. After obtaining the set of non-dominated solutions, a decision maker can use higher level qualitative considerations or implement an automatic decision-making method to make a choice [31].

In this paper, a set of N_{sat} solutions in terms of t_{of} and ΔV is obtained to cover the desired AOI within the maximum assigned time frame, D. While for manoeuvring satellites, t_{of} and ΔV are both computed within the overflight manoeuvre design block, for non-manoeuvring satellites, t_{of} is computed using the overflight analysis block and ΔV is 0. It is worth underlining that the coverage percentage has not been considered as an objective of the optimization algorithm, but rather as a minimum requirement enforced to filter out inadequate overflight solutions. Therefore, the problem addressed in this work is a two-objective optimization where both objectives, i.e., ΔV and t_{of}, are to be minimized, as conceptually shown in Figure 7.

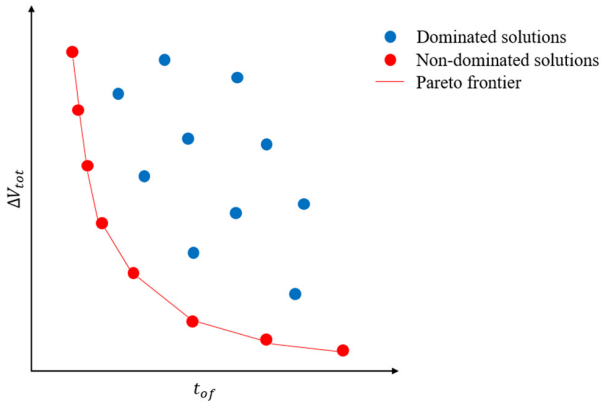


Figure 7. Conceptual representation of dominated solutions, non-dominated solutions, and Pareto frontier for a two-objective optimization problem where the two-optimization objectives are those of interest for the paper, i.e., fuel consumption and time to overflight.

To find a subset of non-dominated solutions to this problem and then to select a single best solution, a multi-attribute decision-making (MADM) method is applied in the optimization block of Figure 1. In general, considering a set of m alternatives, $a_i (i = 1, 2, \ldots, m)$, evaluated with respect to a set of n attributes or criteria, $C_j (j = 1, 2, \ldots, n)$, a decision matrix for m alternatives and n attributes can be defined as in [32]:

$$X = \begin{bmatrix} x_{11} & x_{12} & \cdots_1 & x_{1n} \\ x_{21} & x_{22} & \cdots_1 & x_{2n} \\ \cdots_1^1 & \cdots_1^1 & \cdots_1 & \cdots_1^1 \\ x_{m1} & x_{m2} & \cdots^1 & x_{mn} \end{bmatrix} \tag{19}$$

where x_{ij} stands for the performance value of the $i-th$ alternative in terms of the $j-th$ criterion. A weighting vector representing the relative importance of the attributes can also be set as follows:

$$W = \begin{pmatrix} w_1 & w_2 & \cdots & w_n \end{pmatrix} \tag{20}$$

One of the most widely used MADM techniques is the simple additive weighting (SAW) method, which consists in performing a weighted sum of the performance values of each alternative over all attributes [32]. The SAW method typically requires normalizing the decision matrix X to allow a comparable scale for all its values, as follows.

$$\begin{cases} \bar{r}_{ij} = \frac{x_{ij}}{\max\limits_i x_{ij}} & \text{if } \max\limits_i x_{ij} \text{ is preferable} \\ \bar{r}_{ij} = \frac{\min\limits_i x_{ij}}{x_{ij}} & \text{if } \min\limits_i x_{ij} \text{ is preferable} \end{cases} \tag{21}$$

Therefore, $\bar{r}_{ij}$ $(0 \leq \bar{r}_{ij} \leq 1)$ is defined as the normalized performance value of the $i-th$ alternative when it is evaluated in terms of the $j-th$ criterion. The preference score of each alternative (A_i) can be calculated by Equation (22), as in [32]:

$$A_i = \sum_{j=1}^{n} w_j \bar{r}_{ij} \quad for\ i = 1, 2, \ldots, m \tag{22}$$

The higher the preference score A_i, the more preferable the alternative a_i is. In the case under consideration, the X matrix will have $[m \times 2]$ dimension, where m is the number of satellites, N_{sat}.

$$X = \begin{bmatrix} \Delta V_1 & t_{of_1} \\ \Delta V_2 & t_{of_2} \\ \cdots_1^1 & \cdots_1^1 \\ \Delta V_m & t_{ofm} \end{bmatrix} \tag{23}$$

Since both the ΔV and the t_{of} are to be minimized, the minimum value of the first and second column are considered, ΔV_{min} and $t_{of,min}$, to define the normalized matrix, as follows:

$$\bar{r} = \begin{bmatrix} \overline{\Delta V_1} & \overline{t_{of1}} \\ \overline{\Delta V_2} & \overline{t_{of2}} \\ \cdots & \cdots \\ \overline{\Delta V_m} & \overline{t_{ofm}} \end{bmatrix} \tag{24}$$

where $\overline{\Delta V}_i = \Delta V_{min} / \Delta V_i$ and $\overline{t_{of,i}} = t_{of,min} / t_{of,i}$. It is worth highlighting that when non-manoeuvring overflights lie on the Pareto frontier, the simple additive weighting (SAW) method is applied, considering a ΔV_{min} equal to 10^{-6} km/s to avoid division by 0 in the normalization. Once the ΔV and the t_{of} have been normalized, a pair of weights (w_1, w_2)

is chosen for the ΔV and the t_{of} so that the score for each of the m alternatives can be computed as follows.

$$a_i = \overline{\Delta V_i} w_1 + \overline{t_{of,i}} w_2 \tag{25}$$

Regarding the weights, three options are considered for the numerical performance assessment of the proposed methodology presented in Section 3. First, the ΔV and the t_{of} are considered to be equally important, namely $(w_1, w_2) = (0.5, 0.5)$. Second, an emergency scenario is assumed, giving more importance to the t_{of}, thus having $(w_1, w_2) = (0.4, 0.6)$. Third, a stricter requirement is imposed on fuel consumption, thus setting $(w_1, w_2) = (0.6, 0.4)$. When there is no change in the optimal solution for the pair of weights $(w_1, w_2) = (0.4, 0.6)$ or $(w_1, w_2) = (0.6, 0.4)$, values larger than 0.6 or smaller than 0.4 are considered in the conducted numerical tests.

3. Numerical Results

Three analyses are carried out to validate and assess the proposed methodology. The first analysis considers a set of five simulated LEO satellites, three equipped with an optical sensor and two with a radar; it aims to assess the effect on methodology performance of choosing different AOIs, centred at a mid latitude, at a high latitude, and at a low latitude, respectively. The second analysis considers the same set of five satellites and an AOI centred at a mid latitude; in this case, the performance of the proposed methodology has been evaluated considering three different payload configurations: three satellites equipped with optical sensors and two with radar, all satellites equipped with optical sensors, and all satellites equipped with radar. Finally, the third analysis applies the proposed methodology to a real-world scenario, considering a set of five disaster-monitoring satellites. The three analyses are discussed in the following dedicated subsections.

3.1. Effect of AOI Position

A set of five simulated satellites is defined with the following physical features: m = 850 kg, A_{drag} = 3.86 m^2 and C_d = 2.2. This results in a ballistic coefficient (BC) equal to 0.01 m^2/kg (this is in fact a common value for Earth observation operative satellites [33]). The initial orbital parameters of the simulated satellites are reported in Table 1. In particular, the satellites are assumed to fly on circular orbits (i.e., $e = 0$). The semi-major axis and inclination values have been chosen considering typical orbital characteristics of Earth observation satellites in LEO. The values of the right ascension of the ascending node have been chosen to equally cover the whole interval of [0°, 360°]. Finally, for circular orbits, the initial position of the satellites along their orbits is directly defined through the argument of latitude, u, which has been set equal to 0°. Without losing generality, the orbital parameters of all the satellites are assumed to refer to the same epoch, i.e., 1 July 2019 at 08:00:00.

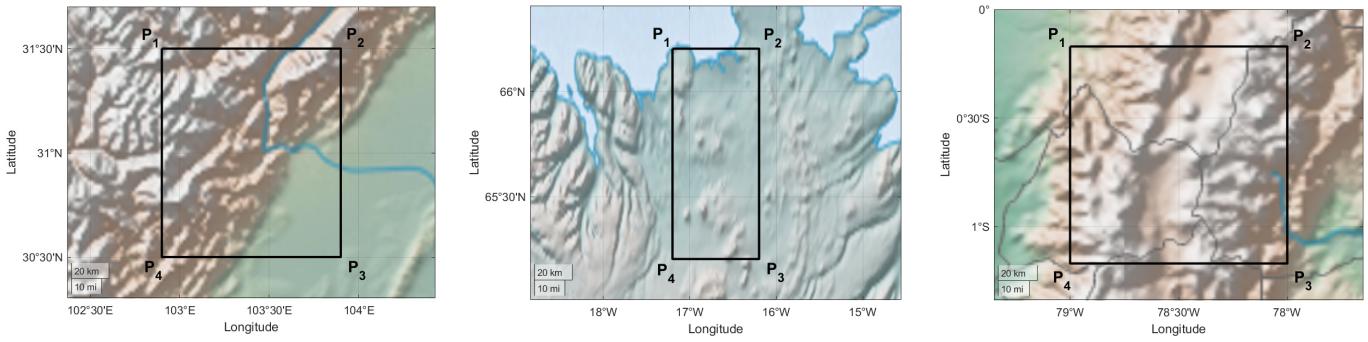
Table 1. Initial orbital elements of the simulated LEO satellites.

Satellite #	a (km)	e (−)	i (°)	Ω (°)	u (°)
1	6828.14	0	97.20	0	0
2	6928.14	0	92.00	72	0
3	7028.14	0	97.99	144	0
4	7128.14	0	71.00	216	0
5	7228.14	0	98.82	288	0

Since most Earth observation satellites are equipped with optical sensors, it is assumed that three out of five satellites are equipped with an optical sensor and two satellites have radar. Specifically, the first, second, and fifth satellites are assumed to be equipped with an

optical sensor with $\alpha = 12°$ and $\beta = 4°$, while the third and fourth satellites instead have an on-board radar with $\gamma = 10°$, $\theta_{min} = 20°$, and $\theta_{max} = 30°$.

The selected AOIs centred at mid, high, and low latitudes are depicted in Figure 8. In the case under consideration, square-shaped AOIs are chosen, characterized by a width of 1° in both latitude and longitude: specifically, the geodetic coordinates of the AOI vertices (P_1, P_2, P_3, and P_4, in clockwise order starting from the upper-left point) are reported in Table 2. The architecture described in Section 2 is applied, setting D to 2 days.



(**a**) (**b**) (**c**)

Figure 8. AOIs at middle (**a**), high (**b**), and low (**c**) latitudes.

Table 2. Geodetic coordinates of AOI vertices at middle, high, and low latitudes.

	$P_1(\lambda_1, \phi_1)$	$P_2(\lambda_2, \phi_2)$	$P_3(\lambda_3, \phi_3)$	$P_4(\lambda_4, \phi_4)$
Mid-latitude AOI	(102.9°, 31.5°)	(103.9°, 31.5°)	(103.9°, 30.5°)	(102.9°, 30.5°)
High-latitude AOI	(−17.2°, 66.2°)	(−16.2°, 66.2°)	(−16.2°, 65.2°)	(−17.2°, 65.2°)
Low-latitude AOI	(−79°, −0.17°)	(−78°, −0.17°)	(−78°, −1.17°)	(−79°, −1.17°)

With regards to the AOI centred at a mid latitude, the results of the proposed architecture are reported in Table 3. For the first, second, and fifth satellites, which are equipped with an optical sensor, illumination conditions have been taken into account. In particular, for the second and fifth satellites, only descending passes have been considered, since ascending passes happen at night. For the first satellite, both ascending and descending passes occur during the daytime; however, the solution occurring in the ascending pass of the first overflight window has been discarded due to a coverage percentage below 30%. For the third and fourth satellites equipped with a radar, solutions with insufficient coverage percentages have been removed. In particular, solutions occurring during the descending pass of the first overflight window and the ascending pass of the second overflight window have been rejected for the third satellite, while solutions corresponding to the ascending and descending pass of the first overflight window have been eliminated for the fourth satellite.

Table 3. ΔV_{tot} and t_{of} for the AOI centred at a mid latitude, considering $D = 2$. Only ascending (A) and descending (D) passages compatible with illumination constraints for optical sensors and with a coverage percentage above 30% are reported.

Satellite #	Day (A/D)	ΔV_{tot} (km/s)	t_{of} (h)	Coverage (%)
1	1 (D)	0.894	2.8	100
	2 (D)	0.0333	24 + 2.8	71.2
	2 (A)	0.0590	24 + 14.2	61.6

Table 3. *Cont.*

Satellite #	Day (A/D)	ΔV_{tot} (km/s)	t_{of} (h)	Coverage (%)
2	1 (D)	10^{-6}	19.3	36.2
	2 (D)	10^{-6}	24 + 19.1	100
3	1 (A)	0.0583	24.0	100
	2 (D)	0.0192	24 + 12.2	91.2
4	2 (A)	0.0315	24 + 5.7	100
	2 (D)	0.0688	24 + 15.5	33.5
5	1 (D)	0.0801	22.1	99.3
	2 (D)	0.0257	24 + 22.1	100

The score evaluation for the subset of non-dominated solutions, which form the Pareto optimal front depicted in Figure 9, is reported in Table 4, considering the three selected sets of weights. As can be seen in Figure 9, there is a non-manoeuvring overflight that lies on the Pareto frontier. By assigning equal weights to ΔV_{tot} and t_{of}, the optimal solution, i.e., the one characterized by a higher score, corresponds to the observation occurring in the descending phase of the first overflight window of the second satellite without the need to manoeuvre and a time to overflight of 19.3 h. Increasing w_1 to 0.6, the non-manoeuvring solution is still the best one. Increasing w_2 to 0.6, the best solution is the one foreseeing a manoeuvre of the first satellite, considering the descending pass of the first overflight window, with a ΔV_{tot} equal to 0.894 km/s and a t_{of} equal to 2.8 h. It is worth noting that although both the non-dominated solutions meet the assigned coverage constraint (i.e., the coverage percentage of candidate solution should always be at least equal to 30%), the optimal solution found when giving more weight to the t_{of}, i.e., the first descending pass of the first satellite, presents a coverage of 100%, while the other one, obtained giving more weight to the ΔV_{tot}, is characterized by a quite low coverage value (36.2%). This is motivated by the fact that the methodology described in Section 2.2 does not take the coverage percentage into account in the multi-objective optimization process.

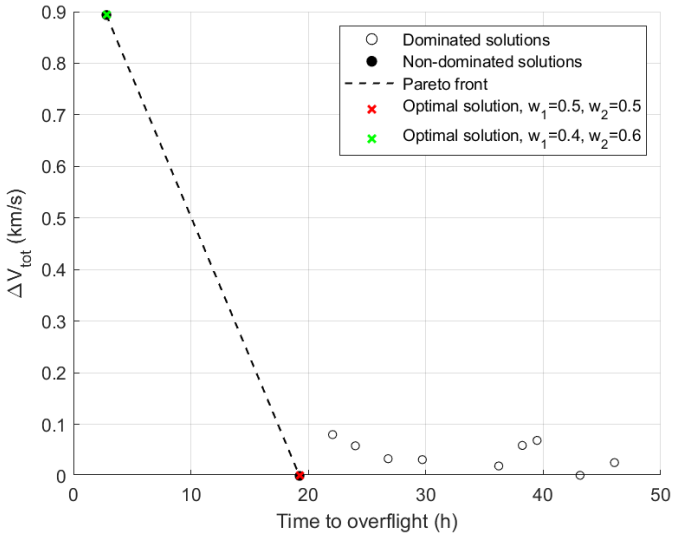


Figure 9. Non-dominated solutions, Pareto frontier, and the optimal solution obtained by applying the SAW method with weights (w_1, w_2) equal to (0.5, 0.5) and (0.4, 0.6) for the area of interest at mid latitudes. Same solution to the former for (w_1, w_2) equal to (0.6, 0.4).

Table 4. Performance score for each non-dominated solution obtained by applying the SAW method for weights pair (w_1, w_2) equal to (0.4, 0.6), (0.5, 0.5), and (0.4, 0.6), when considering the area of interest at mid latitudes.

Satellite #	Day (A/D)	ΔV_{tot} (km/s)	t_{of} (h)	Score		
				$w_1 = 0.4$ $w_2 = 0.6$	$w_1 = 0.5$ $w_2 = 0.5$	$w_1 = 0.6$ $w_2 = 0.4$
1	1 (D)	0.894	2.8	0.600	0.500	0.400
2	1 (D)	10^{-6}	19.3	0.487	0.573	0.658

Results for the case of an AOI centred at a high latitude are synthetized in Table 5. For the first, second, and fifth satellites, which are equipped with an optical sensor, illumination conditions are taken into account. In this case, the ascending and descending passes of the aforementioned satellites take place during the daytime and, thus, there are no discarded solutions due to inadequate illumination conditions. However, for the first satellite, the observation occurring during the descending pass of the first overflight window has been removed due to a coverage percentage below 30%. Similarly, the solutions occurring during ascending passes for the third satellite and those occurring during descending passes for the fourth satellite have been discarded due to too-low coverage percentages.

Table 5. ΔV_{tot} and t_{of} for the area of interest at high latitudes, considering $D = 2$. Only passages (ascending and/or descending) compatible with illumination conditions and with a coverage percentage above 30% are reported.

Satellite #	Day (A/D)	ΔV_{tot} (km/s)	t_{of} (h)	Coverage (%)
1	1 (A)	0.0815	21.4	85.4
	2 (D)	0.0533	24 + 11.6	98.2
	2 (A)	10^{-6}	24 + 21.5	92.1
2	1 (A)	0.430	3.0	39.6
	1 (D)	0.140	15.6	100
	2 (A)	0.0385	24 + 3.0	100
	2 (D)	0.0512	24 + 15.5	100
3	1 (D)	0.101	20.8	59.8
	2 (D)	0.0694	24 + 20.8	90.0
4	1 (A)	10^{-6}	17.0	100
	2 (A)	0.0639	24 + 16.8	60.4
5	1 (D)	0.101	7.0	71.9
	1 (A)	0.140	16.4	63.4
	2 (D)	0.00335	24 + 7.0	82.1
	2 (A)	0.0424	24 + 16.4	81.5

Figure 10 shows the results of the two-objective optimization (i.e., the dominated and non-dominated solutions and the Pareto frontier) as well as the optimal solution obtained by applying the SAW method for pairs of weights $(w_1,\ w_2)$ equal to (0.5, 0.5) and (0.4, 0.6). As can be seen in Figure 10, there is a non-manoeuvring overflight that lies on the Pareto frontier. Table 6 reports the score evaluation for the subset of non-dominated solutions, considering the three selected sets of weights. By assigning equal weights to ΔV_{tot} and t_{of}, the optimal solution corresponds to the observation occurring in the ascending pass of the first overflight window of the fourth satellite, without the need to manoeuvre, which allows us to cover 100% of the AOI. For the pair of weights (0.6, 0.4) the non-manoeuvring solution is still the best one. Increasing the weight assigned to t_{of} to $w_2 = 0.6$, it is advantageous

to manoeuvre the second satellite, considering the ascending pass of the first overflight window. This last solution is instead characterized by a coverage percentage of around 39%.

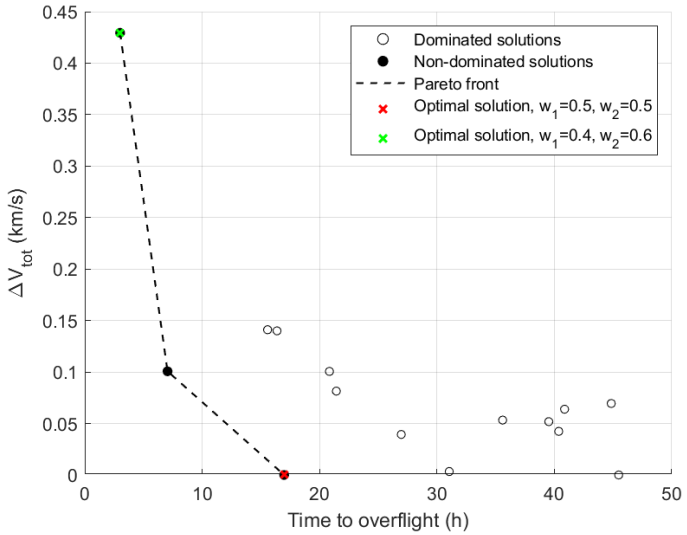


Figure 10. Non-dominated solutions, Pareto frontier, and the optimal solution obtained by applying the SAW method with weights $(w_1,\ w_2)$ equal to (0.5, 0.5) and (0.4, 0.6) for the area of interest at high latitudes. Same solution to the former for $(w_1,\ w_2)$ equal to (0.6, 0.4).

Table 6. Performance score for each non-dominated solution obtained by applying the SAW method for weights pair (w_1, w_2) equal to (0.4, 0.6), (0.5, 0.5), and (0.4, 0.6), when considering the area of interest at high latitudes.

Satellite #	Day (A/D)	ΔV_{tot} (km/s)	t_{of} (h)	Score		
				w_1 = 0.4 w_2 = 0.6	w_1 = 0.5 w_2 = 0.5	w_1 = 0.6 w_2 = 0.4
2	1 (A)	0.430	3.0	0.600	0.500	0.400
4	1 (A)	10^{-6}	17.0	0.506	0.589	0.671
5	1 (D)	0.101	7.0	0.256	0.213	0.171

Table 7 provides the results for the case of an AOI centred at a low latitude. For the first, second, and fifth satellites, which are equipped with optical sensors, only ascending or descending passes are considered depending on the illumination conditions. For the third satellite, on the other hand, only the overflight solution occurring during the descending pass of the second overflight window has been considered, since all other solutions are characterized by coverage percentages below 30%. For the same reason, observations occurring during the ascending and descending pass of the first overflight window have been ignored for the fourth satellite. Furthermore, it can be noticed that there are no non-manoeuvring overflights in this case.

Table 7. ΔV_{tot} and t_{of} for the area of interest at low latitudes, considering $D = 2$. Only passages (ascending and/or descending) compatible with illumination conditions and with a coverage percentage above 30% are reported.

Satellite #	Day (A/D)	ΔV_{tot} (km/s)	t_{of} (h)	Coverage (%)
1	1 (D)	0.0333	14.6	59.8
	2 (D)	0.0737	24 + 14.6	55.9
2	1 (A)	0.192	7.4	39.6
	2 (A)	0.0400	24 + 7.4	72.7

Table 7. *Cont.*

Satellite #	Day (A/D)	ΔV_{tot} (km/s)	t_{of} (h)	Coverage (%)
3	2 (D)	0.0692	24 + 12.4	69.2
4	2 (D)	0.0460	24 + 4.6	56.3
	2 (A)	0.0422	24 + 16.9	99.6
5	1 (D)	0.305	9.8	51.4
	2 (D)	0.0717	24 + 9.8	94.4

Table 8 provides the score evaluation for the subset of non-dominated solutions, which form the Pareto optimal front depicted in Figure 11. The optimal solution obtained by assigning w_1 = 0.5 and w_2 = 0.5 corresponds to the observation occurring in the descending pass of the first overflight window by the first satellite, with ΔV_{tot} = 0.0333 km/s and t_{of} = 14.6 h, which is also the best one in terms of AOI coverage, with a percentage of around 60%. The same solution is obtained not only for $(w_1,\ w_2)$ equal to (0.6, 0.4) but also for $(w_1,\ w_2)$ equal to (0.4, 0.6). Thus, in this case, the weight assigned to w_2 is increased to 0.7 in order to obtain as the optimal solution the one taking place during the ascending pass of the first overflight window by the second satellite, with ΔV_{tot} = 0.192 km/s and time to overflight = 7.4 h.

Table 8. Performance score for each non-dominated solution obtained by applying the SAW method for weights pair (w_1, w_2) equal to (0.3, 0.7), (0.5, 0.5) and (0.4, 0.6), when considering the area of interest at low latitudes.

Satellite #	Day (A/D)	ΔV_{tot} (km/s)	t_{of} (h)	Score		
				w_1 = 0.3 w_2 = 0.7	w_1 = 0.5 w_2 = 0.5	w_1 = 0.6 w_2 = 0.4
1	1 (D)	0.0333	14.6	0.655	0.754	0.803
2	1 (A)	0.192	7.4	0.752	0.587	0.504

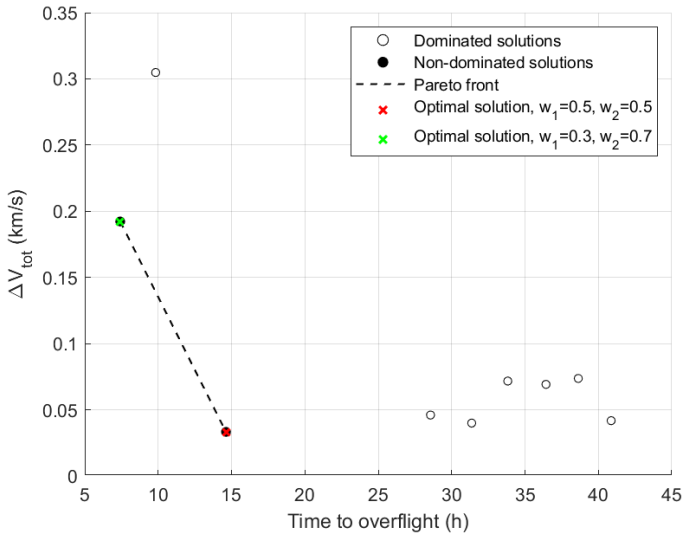


Figure 11. Non-dominated solutions, Pareto frontier, and the optimal solution obtained by applying the SAW method with weights $(w_1,\ w_2)$ equal to (0.5, 0.5) and (0.3, 0.7) for the area of interest at low latitudes. Same solution to the former for $(w_1,\ w_2)$ equal to (0.6, 0.4).

To sum up, the following considerations can be made. The selection of an area of interest at higher latitudes increases the number of satellites that overfly the area of interest without the need for manoeuvring: therefore, the number of satellites requiring

manoeuvring will decrease, but the manoeuvred subset does not show any appreciable variations in ΔV_{tot} and t_{of}. Both at high and mid latitudes, the manoeuvring solution is favoured only if a stricter requirement is posed on responsiveness (i.e., $w_2 = 0.6$). In the present case, the number of solutions given as input to the optimization algorithm is greater for the area of interest at high latitudes. Indeed, for satellites equipped with an optical sensor, the number of solutions under consideration increases as the latitude increases, since the selected initial epoch is 1 July 2019.

3.2. Effect of Different Payload Configurations

The second analysis is conducted considering the same set of simulated satellites as those in Section 3.1. Three different payload configurations have been considered: three satellites equipped with an optical sensor and two with a radar (case A), all satellites equipped with an optical sensor (case B), and all satellites equipped with a radar (case C). The same specifications as in Section 3.1 are set for the optical and radar sensors.

The chosen AOI—whose vertices have the following geodetic coordinates: P_1 ($\lambda = 13.7°$, $\phi = 41.15°$), P_2 ($\lambda = 14.7°$, $\phi = 41.15°$), P_3 ($\lambda = 14.7°$, $\phi = 40.55°$), and P_4 ($\lambda = 13.7°$, $\phi = 40.55°$)—is depicted in Figure 12. D is again set equal to 2 days.

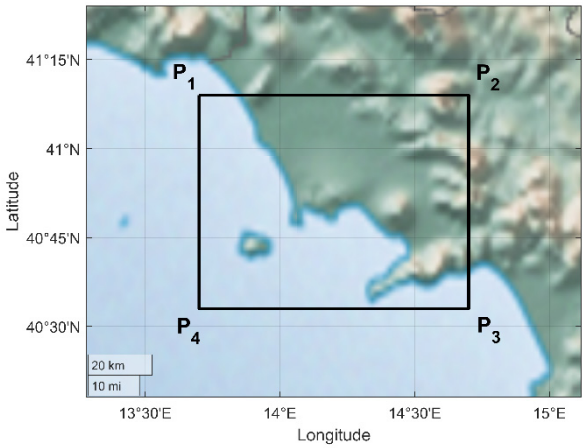


Figure 12. AOI chosen for the second test case.

Results for case A are reported in Table 9. Specifically, it is assumed that the first, second, and fifth satellites mount optical sensors, while the third and fourth satellites are equipped with a radar. For the second and the fifth satellites, only ascending or descending passes have been considered depending on the illumination conditions. For the first satellite, on the other hand, all the observations happen during the daytime; however, the solution occurring during the descending pass of the first overflight window has been discarded due to the inadequate coverage percentage. For the third satellite, the observation occurring during the ascending pass of the first overflight window has not been considered, since it is characterized by a coverage percentage below 30%. For the same reason, solutions happening during the ascending and descending pass of the first overflight window have been discarded for the fourth satellite.

Table 9. ΔV_{tot} and t_{of} for case A, considering $D = 2$. Only passages (ascending and/or descending) compatible with illumination conditions and with a coverage percentage above 30% are reported.

Satellite #	Day (A/D)	ΔV_{tot} (km/s)	t_{of} (h)	Coverage (%)
1	1 (A)	0.0526	20.0	66.0
	2 (D)	0.0361	24 + 8.9	78.6
	2 (A)	0.0773	24 + 20.0	63.6

Table 9. *Cont.*

Satellite #	Day (A/D)	ΔV_{tot} (km/s)	t_{of} (h)	Coverage (%)
2	1 (A)	1.671	1.1	100
	2 (A)	0.0597	24 + 1.1	73.3
3	1 (D)	0.0375	18.3	77.9
	2 (A)	0.107	24 + 5.8	33.0
	2 (D)	0.0405	24 + 18.3	76.4
4	2 (A)	0.0542	24 + 12.0	92.9
	2 (D)	0.0291	24 + 21.0	86.4
5	1 (D)	0.909	4.2	100
	2 (D)	0.118	24 + 4.2	99.8

Table 10 provides the score evaluation for the subset of non-dominated solutions, which form the Pareto optimal front shown in Figure 13, considering the three selected sets of weights. The best solution obtained by applying the SAW method with $w_1 = 0.5$ and $w_2 = 0.5$ corresponds to the observation occurring in the descending pass of the second overflight window by the fourth satellite, with a time to overflight of 45 h and $\Delta V_{tot} = 0.0291$ km/s. This solution is obviously confirmed as the best for the pair of weights equal to (0.6, 0.4). The coverage percentage of this overflight is 86.4%. Instead, when assigning more weight to the overflight time ($w_2 = 0.6$), it is advantageous to manoeuvre the second satellite considering the ascending pass of the first overflight window with a $\Delta V_{tot} = 1.671$ km/s and a time to overflight of 1.1 h, which also correspond to a 100% coverage of the AOI.

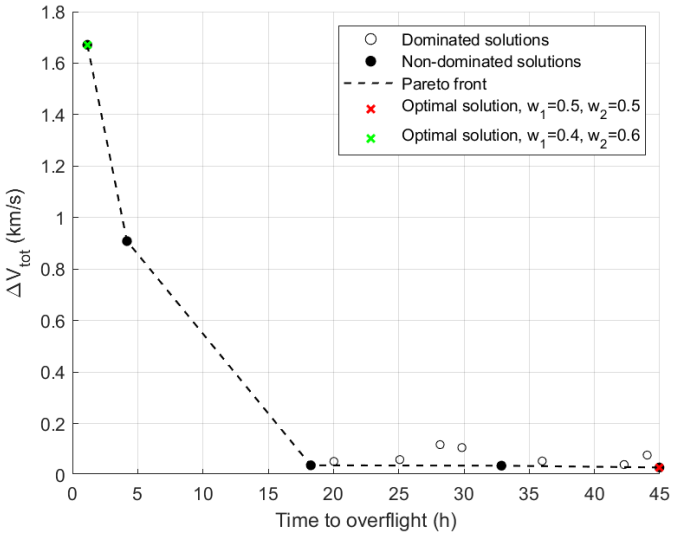


Figure 13. Non-dominated solutions, Pareto frontier, and the optimal solution obtained by applying the simple additive weighting method with weights (w_1, w_2) equal to (0.5, 0.5) and (0.4, 0.6), with 3 satellites equipped with an optical sensor and 2 satellites equipped with a radar sensor. Same solution to the former for (w_1, w_2) equal to (0.6, 0.4).

Table 10. Performance score for each non-dominated solution obtained by applying the SAW method for weights pair (w_1, w_2) equal to (0.4, 0.6), (0.5, 0.5), and (0.4, 0.6), when considering case A.

Satellite #	Day (A/D)	ΔV_{tot} (km/s)	t_{of} (h)	Score		
				$w_1 = 0.4$ $w_2 = 0.6$	$w_1 = 0.5$ $w_2 = 0.5$	$w_1 = 0.6$ $w_2 = 0.4$
1	2 (D)	0.0361	24 + 8.9	0.343	0.421	0.498

Table 10. *Cont.*

Satellite #	Day (A/D)	ΔV_{tot} (km/s)	t_{of} (h)	Score		
				$w_1 = 0.4$ $w_2 = 0.6$	$w_1 = 0.5$ $w_2 = 0.5$	$w_1 = 0.6$ $w_2 = 0.4$
2	1 (A)	1.671	1.1	0.607	0.509	0.410
3	1 (D)	0.0375	18.3	0.348	0.420	0.491
4	2 (D)	0.0291	24 + 21.0	0.415	0.513	0.610
5	1 (D)	0.909	4.2	0.177	0.153	0.128

With regards to case B, the results of the proposed architecture are reported in Table 11. For the second, third, fourth, and fifth satellites, only ascending or descending passes have been considered depending on the illumination conditions. For the first satellite, on the other hand, all overflights take place during the daytime; however, the descending pass of the first overflight window has been discarded due to the insufficient coverage percentage.

Table 11. ΔV_{tot} and t_{of} for case B, considering $D = 2$. Only passages (ascending and/or descending) compatible with illumination conditions and with a coverage percentage above 30% are reported.

Satellite #	Day (A/D)	ΔV_{tot} (km/s)	t_{of} (h)	Coverage (%)
1	1 (A)	0.0526	20.0	66.0
	2 (D)	0.0361	24 + 8.9	78.6
	2 (A)	0.0773	24 + 20.0	63.6
2	1 (A)	1.671	1.1	100
	2 (A)	0.0597	24 + 1.1	73.4
3	1 (A)	0.499	5.6	43.4
	2 (A)	0.00841	24 + 5.6	99.2
4	1 (D)	0.0867	21.5	93.0
	2 (D)	0.104	24 + 21.3	94.9
5	1 (D)	0.909	4.2	100
	2 (D)	0.118	24 + 4.2	99.8

Table 12 reports the score evaluation for the subset of non-dominated solutions depicted in Figure 14, considering the three selected sets of weights. By assigning equal weight to ΔV_{tot} and t_{of}, the optimal solution corresponds to the observation occurring in the ascending pass of the second overflight window by the third satellite, with a time to overflight of 29.6 h and ΔV_{tot} = 0.00841 km/s. The same solution is obtained for the pair of weights (0.6, 0.4). Increasing the weight assigned to t_{of} to 0.6, it is preferable to manoeuvre the second satellite, considering the ascending pass of the first overflight window, with a time to overflight of 1.1 h and ΔV_{tot} = 1.671 km/s. In this case, both the solutions present high values of coverage percentage.

Table 12. Performance score for each non-dominated solution obtained by applying the SAW method for weights pair (w_1, w_2) equal to (0.4, 0.6), (0.5, 0.5), and (0.4, 0.6), when considering case B.

Satellite #	Day (A/D)	ΔV_{tot} (km/s)	t_{of} (h)	Score		
				$w_1 = 0.4$ $w_2 = 0.6$	$w_1 = 0.5$ $w_2 = 0.5$	$w_1 = 0.6$ $w_2 = 0.4$
1	1 (A)	0.0526	20.0	0.0982	0.108	0.119
2	1 (A)	1.671	1.1	0.602	0.503	0.403
3	1 (A)	0.499	5.6	0.129	0.111	0.0918
	2 (A)	0.00841	24 + 5.6	0.423	0.519	0.615
5	1 (D)	0.909	4.2	0.168	0.141	0.115

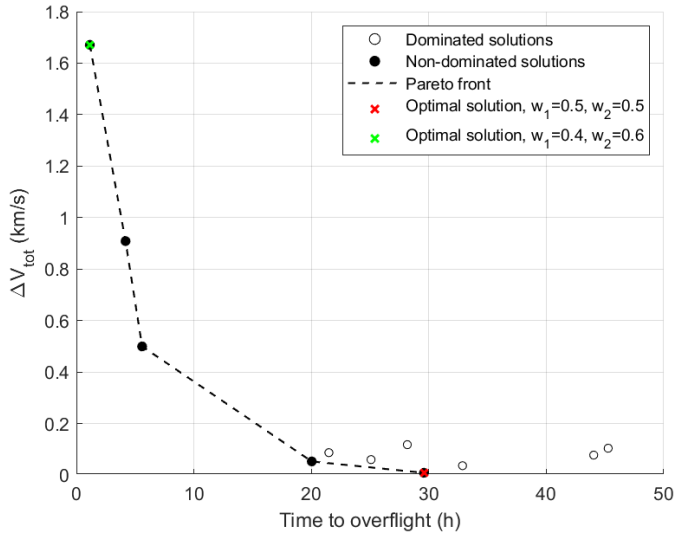


Figure 14. Non-dominated solutions, Pareto frontier, and the optimal solution obtained by applying the SAW method with weights (w_1, w_2) equal to (0.5, 0.5) and (0.4, 0.6), with all satellites equipped with an optical sensor. Same solution to the former for (w_1, w_2) equal to (0.6, 0.4).

Table 13 provides the results of the proposed architecture for case C. Solutions with a coverage percentage below 30% have been discarded. In particular, for the first satellite, solutions occurring during the descending passes of the first and second overflight windows have been eliminated. For the second and third satellites, however, the solution occurring during the ascending pass of the first overflight window has been discarded. For the fourth satellite, solutions occurring during the ascending and descending passes of the first overflight window have been deleted. Finally, for the fifth satellite, solutions occurring during the ascending and descending passes of the first overflight window and the ascending pass of the second overflight window have been rejected.

Table 13. ΔV_{tot} and t_{of} for case C, considering $D = 2$. Only passages (ascending and/or descending) with a coverage percentage above 30% are reported.

Satellite #	Day (A/D)	ΔV_{tot} (km/s)	t_{of} (h)	Coverage (%)
1	1 (A)	0.0301	20.2	99.0
	2 (A)	0.0671	24 + 20.2	55.1
2	1 (D)	0.0457	13.1	52.0
	2 (A)	0.0383	24 + 1.3	100
	2 (D)	0.0121	24 + 13.1	95.4
3	1 (D)	0.0375	18.3	77.7
	2 (A)	0.107	24 + 5.8	33.8
	2 (D)	0.0405	24 + 18.3	76.6
4	2 (A)	0.0542	24 + 12.0	93.3
	2 (D)	0.0291	24 + 21.0	86.5
5	2 (D)	0.1335	24 + 4.0	64.5

Figure 15 shows the results of the two-objective optimization, namely the dominated and non-dominated solutions and the Pareto frontier, as well as the optimal solution obtained by applying the SAW method for pairs of weights (w_1, w_2) equal to (0.5, 0.5) and (0.4, 0.6). Table 14 reports the score evaluation for the subset of non-dominated solutions, considering the three selected sets of weights. By assigning equal weight to ΔV_{tot} and t_{of}, the best solution corresponds to the overflight that occurs in the descending pass of the second overflight window by the second satellite, with a time to overflight of 37.1 h and

ΔV_{tot} = 0.0121 km/s. Increasing the weight assigned to ΔV_{tot} to 0.6, this solution is still the best one. Instead, when increasing the weight assigned to t_{of} to 0.6, it is advantageous to manoeuvre the second satellite, considering the descending pass of the first overflight window, with a time to overflight of 13.1 h and ΔV_{tot} = 0.0457 km/s. Here, the solution occurring in the second overflight window presents a higher coverage percentage (95.4%) with respect to the one occurring in the first window (52%).

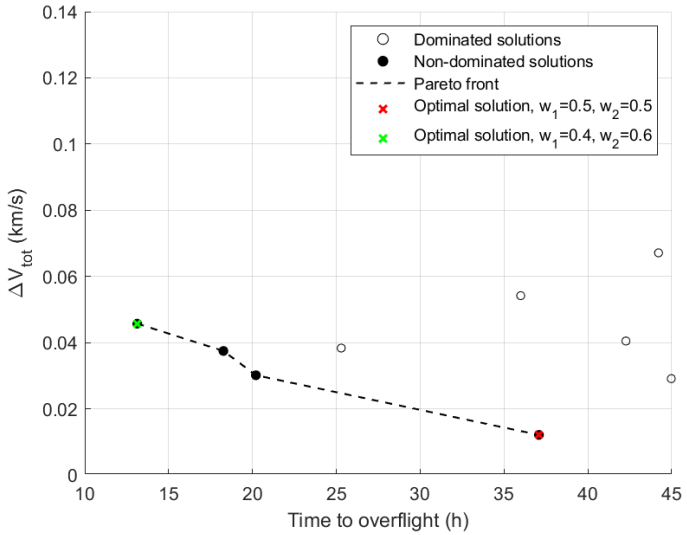


Figure 15. Non-dominated solutions, Pareto frontier, and the optimal solution obtained by applying the SAW method with w_1 = 0.5 and w_2 = 0.5, and w_1 = 0.4 and w_2 = 0.6, with all satellites equipped with a radar. Same results as the former for the pair of weights (0.6, 0.4).

Table 14. Performance score for each non-dominated solution obtained by applying the SAW method for weights pair (w_1, w_2) equal to (0.4, 0.6), (0.5, 0.5), and (0.4, 0.6), when considering case C.

Satellite #	Day (A/D)	ΔV_{tot} (km/s)	t_{of} (h)	Score		
				w_1 = 0.4 w_2 = 0.6	w_1 = 0.5 w_2 = 0.5	w_1 = 0.6 w_2 = 0.4
1	1 (A)	0.0301	20.2	0.551	0.526	0.501
2	1 (D)	0.0457	13.1	0.706	0.632	0.559
	2 (D)	0.0121	24 + 13.1	0.612	0.677	0.742
3	1 (D)	0.0375	18.3	0.560	0.521	0.481

To sum up, the following considerations can be made. By considering different payload configurations, the overflight solutions obtained from the overflight manoeuvre design block do not show any appreciable variations in ΔV_{tot} and t_{of}. For satellites equipped with an optical sensor, some overflight solutions have been discarded not only depending on the obtained coverage percentage, but also depending on the illumination conditions and, thus, the latitude of the area of interest and the selected initial epoch. For satellites equipped with a radar, on the other hand, solutions that have been eliminated are those characterized by a coverage percentage below 30%. Even though the number of overflight solutions given as input to the optimization algorithm can change depending on the payload configuration, the type of on-board sensors does not significantly affect the optimization results.

3.3. Real Test Case

Finally, the proposed methodology is applied to a set of five real satellites for disaster monitoring. Table 15 provides the orbital parameters and the initial epoch of each satellite obtained from True Line Element (TLE) sets, dated 17 November 2023 [34]. Since each TLE

set corresponds to a slightly different epoch, the satellites' trajectories are first propagated up to the latest one to obtain the initial conditions of the analysis. All the satellites fly on a sun-synchronous orbit. With the exception of RISAT-1 that has an on-board radar, all the other satellites are equipped with optical sensors. The specifications of the on-board sensors, listed in Table 16, are taken from [35–39].

Table 15. Orbital elements and epoch of the disaster-monitoring satellite.

Satellite	a (km)	e (−)	i (°)	Ω (°)	ω (°)	ν (°)	Epoch
Deimos-1	7030.2	0.000197	97.68	149.94	40.30	40.18	17/11/2023 12:22:15.468
UK-DMC 2	7031.0	0.000156	97.752	113.37	82.76	82.64	17/11/2023 10:29:19.671
RISAT 1	6887.1	0.000140	97.54	333.87	268.36	91.77	17/11/2023 11:58:11.794
HJ-1B	7009.2	0.00397	97.64	338.56	32.90	32.78	17/11/2023 10:42:15.455
DMC3-FM2	6997.8	0.000623	97.78	202.27	273.90	86.22	17/11/2023 12:03:18.755

Table 16. FOV along the cross-track α and tangential β directions for satellites equipped with an optical sensor; in-track angle γ, minimum, θ_{min}, and maximum, θ_{max}, off-nadir angles for satellite equipped with a radar.

	(α,β)	$(\gamma,\theta_{min},\theta_{max})$
Deimos-1	(51.6°, 12.9°)	-
UK-DMC 2	(51.5°, 12.9°)	-
RISAT 1	-	(10°, 10°, 49°)
HJ-1B	(57.2°, 14.3°)	-
DMC3-FM2	(2.0°, 0.5°)	-

The AOI, shown in Figure 16, is Port-au-Prince in Haiti, which experienced a strong earthquake in 2010. The vertices of the rectangular AOI are P_1 ($\lambda = -73.0°$, $\phi = 19.0°$), P_2 ($\lambda = -72.0°$, $\phi = 19.0°$), P_3 ($\lambda = -72.0°$, $\phi = 18.0°$), and P_4 ($\lambda = -73.0°$, $\phi = 18.0°$).

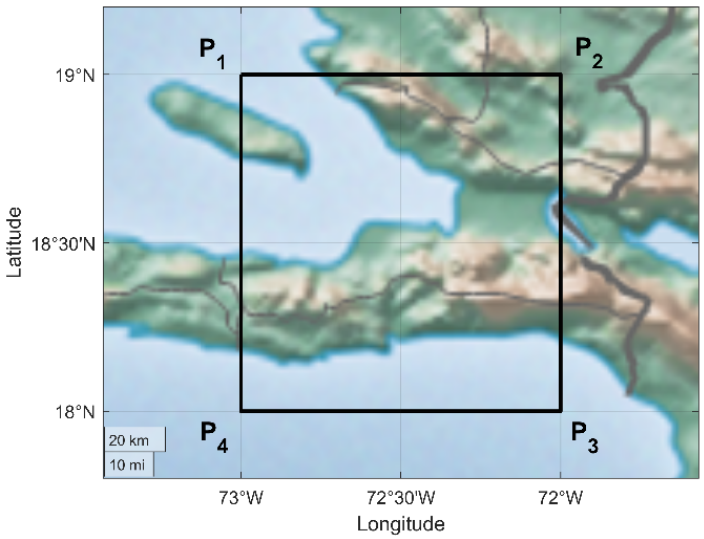


Figure 16. AOI of the real test case scenario.

Table 17 shows the results for the set of disaster-monitoring satellites. For the fifth satellite, all solutions have been discarded because they exhibit coverage percentages below 30% due to the small FOV. For the first, second, and fourth satellites equipped with an optical sensor, only ascending or descending passes are considered, depending on the illumination conditions. For the third radar-equipped satellite, on the other hand, the

solution occurring during the ascending pass of the first overflight window has been deleted due to the inadequate coverage percentage.

Table 17. ΔV_{tot} and t_{of} for each satellite of the real scenario set. Only passages (ascending and/or descending) compatible with illumination conditions and with a coverage percentage above 30% are reported.

Satellite #	Day (A/D)	ΔV_{tot} (km/s)	t_{of} (h)	Coverage (%)
1	1 (A)	0.00825	22.5	100
	2 (A)	0.0322	24 + 22.5	100
2	1 (D)	0.318	8.5	71.8
	2 (D)	0.118	24 + 8.5	100
3	1 (D)	0.125	22.9	98.2
	2 (A)	0.0630	24 + 11.1	73.6
	2 (D)	0.0428	24 + 22.9	100
4	1 (D)	0.142	23.5	100
	2 (D)	0.00563	24 + 23.5	100

Figure 17 shows the results of the two-objective optimization: the dominated and non-dominated solutions and the Pareto frontier as well as the optimal solution obtained by applying the SAW method for pairs of weights (w_1, w_2) equal to (0.5, 0.5) and (0.4, 0.6). The score evaluation for the subset of non-dominated solutions is reported in Table 18, considering the three selected sets of weights. By assigning equal weight to ΔV_{tot} and t_{of}, the optimal solution corresponds to the overflight obtained by manoeuvring the fourth satellite and considering the descending pass of the second overflight window, with ΔV_{tot} = 0.00563 km/s and t_{of} = 47.5 h. This solution is still the best one by increasing the weight assigned to the ΔV_{tot} to 0.6. Instead, when assigning more weight to the time to overflight (w_2 = 0.6), it is preferable to manoeuvre the second satellite considering the descending pass of the first overflight window, with ΔV_{tot} = 0.318 km/s and time to overflight = 8.5 h. This last solution provides a coverage of 71.8%, while the first one allows covering the whole AOI.

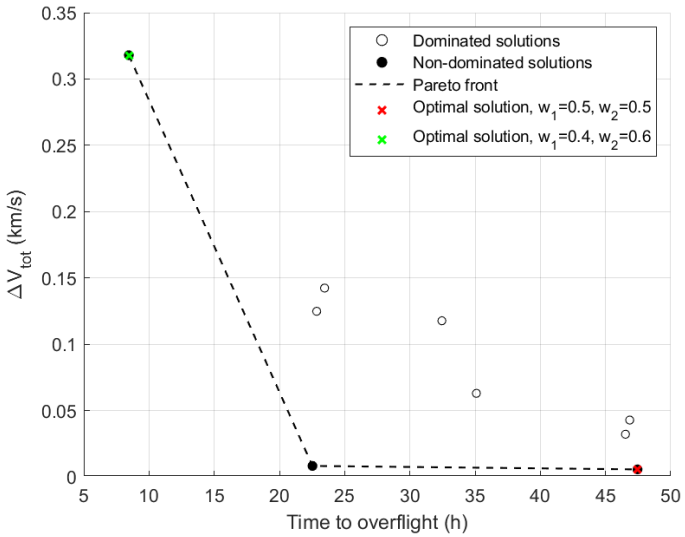
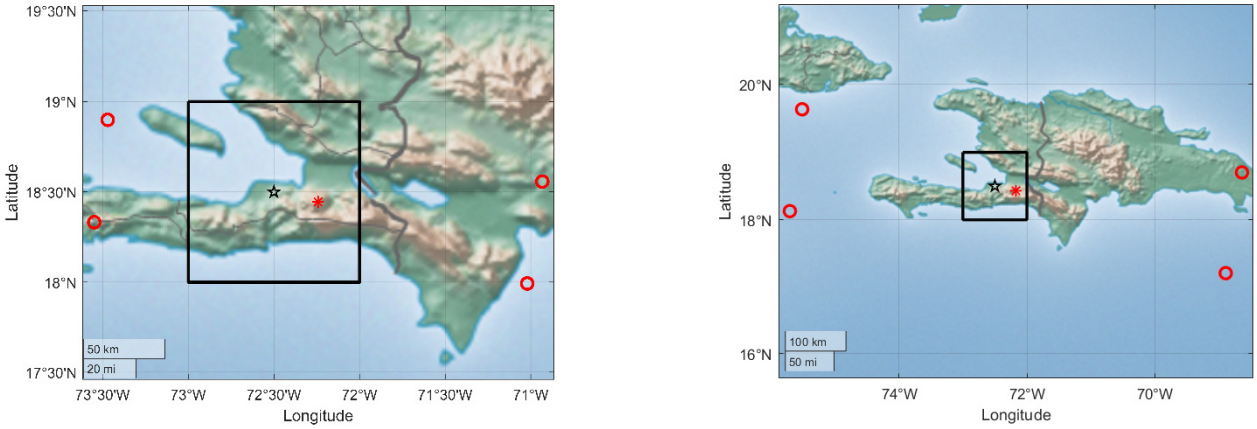


Figure 17. Dominated solutions, non-dominated solutions, Pareto frontier, and the optimal solution obtained by applying the SAW method with w_1 = 0.5 and w_2 = 0.5, and w_1 = 0.4 and w_2 = 0.6 for t_{of} = 2 days in a real test case scenario. Same results as the former for (0.6, 0.4).

Table 18. Performance score for each non-dominated solution obtained by applying the SAW method for weights pair (w_1, w_2) equal to (0.4, 0.6), (0.5, 0.5), and (0.4, 0.6), when considering the real test case scenario.

Satellite #	Day (A/D)	ΔV_{tot} (km/s)	t_{of} (h)	Score		
				$w_1 = 0.4$ $w_2 = 0.6$	$w_1 = 0.5$ $w_2 = 0.5$	$w_1 = 0.6$ $w_2 = 0.4$
1	1 (A)	0.00825	22.5	0.498	0.529	0.560
2	1 (D)	0.318	8.5	0.607	0.509	0.411
4	2 (D)	0.00563	24 + 23.5	0.507	0.589	0.671

Figure 18 illustrates the observation made by the second satellite considering the descending pass of the first overflight window and the observation made by the fourth satellite considering the descending pass of the second overflight window. In both cases, the footprints are depicted at the instant of time when the distance between the barycentre of the footprint and the barycentre of the area of interest is the smallest. As shown in Figure 18, the footprint of the manoeuvred satellites intersects the AOI and, thus, it is observable. However, the barycentre of the footprint does not have the same coordinates as the barycentre of the AOI. This happens because the analytical model used to evaluate the required manoeuvre to overfly the area of interest uses a different model to describe the rotation of the Earth than the one used to verify whether the overflight occurs.



(**a**) (**b**)

Figure 18. Footprint of the manoeuvred satellite at the point of minimum distance between the barycentre of the footprint and the barycentre of the area of interest for (w_1, w_2) equal to (0.4, 0.6) (**a**) and for (w_1, w_2) equal to (0.5, 0.5) and (0.6, 0.4) (**b**). The empty dots are the vertices of the footprint, and the asterisk is the sub-satellite point. Black lines mark the area of interest, and the black star represents the barycentre of the area of interest.

4. Conclusions

This paper proposes a decision-making architecture to select the optimal manoeuvre that enables a set of multiple sensor-equipped satellites to overfly a specified area of interest within a certain maximum time to the expected overflight. This architecture is composed of three main blocks. The overflight block enables us to check whether any satellite overflies the AOI without the need for manoeuvring within the required time. For the subset of satellites that do not overfly the AOI, the manoeuvre design block is activated. A dual coplanar impulsive manoeuvre is designed by modifying a state-of-the-art analytical J_2-perturbed model to account for on-board sensors (i.e., optical and radar) and an extended (non-punctual) AOI. Once the overflight solutions in terms of ΔV_{tot} (equal to 0 km/s for non-manoeuvring satellites) and time to overflight are computed for each satellite of the

initial set, an optimization block is implemented to determine which satellite to manoeuvre. A multi-objective optimization problem is solved to find a set of equally optimal solutions (i.e., non-dominated solutions) that form the Pareto optimal front. Then, the additive weighting method is applied to select the best solution according to the decision-making preferences. The proposed architecture has been validated by considering both simulated and real test cases. In the former case, different scenarios have been simulated varying the type of on-board sensors and the AOI. When considering areas of interest at different latitudes, the results showed that the number of obtained non-manoeuvring solutions is greater for mid- or high-latitude AOIs. Furthermore, the number of solutions provided as input to the optimization algorithm is higher when considering a high-latitude area of interest, as the initial epoch selected is 1 July 2019. The number of solutions given as input to the optimization algorithm also changes according to the different types of on-board sensors. Indeed, while for satellites equipped with a radar, solutions are discarded according to the obtained coverage percentage, for satellites equipped with an optical sensor, solutions are discarded not only according to the obtained coverage percentage but also according to the illumination conditions. In the latter case, a set of real Earth-observation satellites has been considered. In both cases, the proposed architecture outputs an optimal solution, which assures a rapid and efficient overflight of the area of interest. Specifically, the results showed that the optimal manoeuvre enables a timely overflight in less than 15 h if more weight is given to overflight time, while it requires a ΔV_{tot} of about 10^{-2} km/s if more is given to fuel consumption.

Several aspects could be addressed and improved in future works. In particular, attitude manoeuvres could be considered to increase the number of overflights and/or achieve better AOI coverage. Moreover, other optimization objectives, such as the minimum overflight duration, AOI coverage percentage, and pointing/attitude angles required for overflight (e.g., penalizing significant attitude manoeuvres), could be easily considered thanks to the flexibility of the optimization algorithm. Finally, orbital perturbations (and possible a priori known maintenance strategies) could be included to finetune the manoeuvres, e.g., through numerical optimization.

Author Contributions: Conceptualization, A.A., N.C., G.I., R.O. and G.F.; methodology, A.A., N.C., G.I., R.O. and G.F.; software, A.A.; validation, A.A., N.C., G.I., R.O. and G.F.; formal analysis, A.A., N.C., G.I., R.O. and G.F.; investigation, A.A., N.C., G.I., R.O. and G.F.; writing—original draft preparation, A.A.; writing—review and editing, N.C., G.I., R.O. and G.F.; visualization, A.A. and N.C.; supervision, R.O. and G.F. All authors have read and agreed to the published version of the manuscript.

Funding: This research received no external funding.

Data Availability Statement: The original contributions presented in this study are included in the article. Further inquiries can be directed to the corresponding author.

Conflicts of Interest: The authors declare no conflicts of interest.

References

1. McGrath, C.N.; Clark, R.A.; Macdonald, M. Novel Concept of Satellite Manoeuvre Planning Using Graph Theoretical Techniques. *Adv. Space Res.* **2021**, *67*, 3775–3784. [CrossRef]
2. Sheng, J.; Geng, Y. Normalized Nodal Distance-Based J2-Perturbed Ground-Track Adjustment with Apsidal-Altitude Constraints. *Aerosp. Sci. Technol.* **2023**, *140*, 108418. [CrossRef]
3. Li, T.; Xiang, J.; Wang, Z.; Zhang, Y. Circular Revisit Orbits Design for Responsive Mission over a Single Target. *Acta Astronaut.* **2016**, *127*, 219–225. [CrossRef]
4. Abdelkhalik, O. Initial Orbit Design from Ground Track Points. *J. Spacecr. Rocket.* **2010**, *47*, 202–205. [CrossRef]

5. Abdelkhalik, O.; Mortari, D. Orbit Design for Ground Surveillance Using Genetic Algorithms. *J. Guid. Control Dyn.* **2006**, *29*, 1231–1235. [CrossRef]
6. Lin, X.; Zhang, G.; Zhang, H. Multi-Target Ground-Track Adjustment with a Single Coplanar Impulse. *Aerosp. Sci. Technol.* **2021**, *119*, 107135. [CrossRef]
7. Co, T.; Black, J.; Zagaris, C. Responsive Satellites Through Ground Track Manipulation Using Existing Technology. *J. Spacecr. Rocket.* **2011**, *50*. [CrossRef]
8. Zhang, G.; Cao, X. Coplanar Ground-Track Adjustment Using Time Difference. *Aerosp. Sci. Technol.* **2016**, *48*, 21–27. [CrossRef]
9. Zhang, G.; Cao, X.; Mortari, D. Analytical Approximate Solutions to Ground Track Adjustment for Responsive Space. *IEEE Trans. Aerosp. Electron. Syst.* **2016**, *52*, 1366–1383. [CrossRef]
10. Zhang, G.; Sheng, J. Impulsive Ground-Track Adjustment for Assigned Final Orbit. *J. Spacecr. Rocket.* **2016**, *53*, 1–11. [CrossRef]
11. Co, T.; Black, J. Responsiveness in Low Orbits Using Electric Propulsion. *J. Spacecr. Rocket.* **2012**, *51*. [CrossRef]
12. Guelman, M.; Shiryaev, A. Closed-Loop Control of Earth Observation Satellites. *J. Spacecr. Rocket.* **2018**, *56*, 1–9. [CrossRef]
13. Mok, S.-H.; Bang, H. Optimal Multi-Target Overflight Using Ground-Track Adjustment. *J. Astronaut. Sci.* **2021**, *68*. [CrossRef]
14. Yu, X.; Liu, K.; Chen, Q. Constellation Design for Responsive Visiting Based on Ground Track Adjustment. *Proc. Inst. Mech. Eng. G J. Aerosp. Eng.* **2017**, *232*, 095441001771647. [CrossRef]
15. de Weck, O.L.; Scialom, U.; Siddiqi, A. Optimal Reconfiguration of Satellite Constellations with the Auction Algorithm. *Acta Astronaut.* **2008**, *62*, 112–130. [CrossRef]
16. Mcgrath, C.; Macdonald, M. General Perturbation Method for Satellite Constellation Reconfiguration Using Low-Thrust Maneuvers. *J. Guid. Control Dyn.* **2019**, *42*, 1–17. [CrossRef]
17. Kandepi, R.; Saini, H.; George, R.K.; Konduri, S.; Karidhal, R. Agile Earth Observation Satellite Constellations Scheduling for Large Area Target Imaging Using Heuristic Search. *Acta Astronaut.* **2024**, *219*, 670–677. [CrossRef]
18. Wang, X.; Wu, G.; Xing, L.; Pedrycz, W. Agile Earth Observation Satellite Scheduling Over 20 Years: Formulations, Methods, and Future Directions. *IEEE Syst. J.* **2020**, *15*, 3881–3892. [CrossRef]
19. Zhang, Z.; Zhang, N.; Jiao, Y.; Baoyin, H.; Li, J. Multitree Search for Multisatellite Responsiveness Scheduling Considering Orbital Maneuvering. *IEEE Trans. Aerosp. Electron. Syst.* **2022**, *58*, 2206–2217. [CrossRef]
20. Zhang, N.; Zhang, Z.; Jiao, Y.; Baoyin, H. Multitrajectory Combination for Multiple Ground Target Observation by Maneuvering On-Orbit Satellites. *IEEE Trans. Aerosp. Electron. Syst.* **2023**, *59*, 8428–8438. [CrossRef]
21. Du, Y.; Wang, T.; Xin, B.; Wang, L.; Chen, Y.; Xing, L. A Data-Driven Parallel Scheduling Approach for Multiple Agile Earth Observation Satellites. *IEEE Trans. Evol. Comput.* **2019**, *24*, 679–693. [CrossRef]
22. Luo, Q.; Peng, W.; Wu, G.; Xiao, Y. Orbital Maneuver Optimization of Earth Observation Satellites Using an Adaptive Differential Evolution Algorithm. *Remote Sens.* **2022**, *14*, 1966. [CrossRef]
23. Yin, Q.; Wu, G.; Sun, G.; Gu, Y. Multi-Objective Orbital Maneuver Optimization of Multi-Satellite Using an Adaptive Feedback Learning NSGA-II. *Swarm Evol. Comput.* **2025**, *93*, 101835. [CrossRef]
24. Lagona, E.; Hilton, S.; Afful, A.; Gardi, A.; Sabatini, R. Autonomous Trajectory Optimisation for Intelligent Satellite Systems and Space Traffic Management. *Acta Astronaut.* **2022**, *194*, 185–201. [CrossRef]
25. Bonnet, J. Multi-Criteria and Multi-Objective Dynamic Planning by Self-Adaptive Multi-Agent System, Application to Earth Observation Satellite Constellations. Ph.D. Thesis, Université Paul Sabatier-Toulouse III, Toulouse, France, 2017.
26. Cimmino, N.; Argirò, A.; Isoletta, G.; Opromolla, R.; Fasano, G. Optimized Multi-Satellite Manoeuvring Strategy for Responsive Earth Observation. In Proceedings of the Aerospace Europe Conference, Joint 10th EUCASS—9th CEAS Conference, Lausanne, Switzerland, 13 July 2023.
27. Maling, D.H. *Coordinate Systems and Map Projections*, 2nd ed.; Pergamon: Oxford, UK, 1992.
28. Montenbruck, O.; Pfleger, T. *Astronomy on the Personal Computer*; Springer: Berlin/Heidelberg, Germany, 2000; p. 1, ISBN 3-540-67221-4.
29. Lim, W. Shoelace Formula: Connecting the Area of a Polygon and Vector Cross Product. *Math. Teach.* **2017**, *110*, 631–636. [CrossRef]
30. Konak, A.; Coit, D.W.; Smith, A.E. Multi-Objective Optimization Using Genetic Algorithms: A Tutorial. *Reliab. Eng. Syst. Saf.* **2006**, *91*, 992–1007. [CrossRef]
31. Deb, K. Multi-Objective Optimization. In *Search Methodologies: Introductory Tutorials in Optimization and Decision Support Techniques*, 2nd ed.; Springer US: New York, NY, USA, 2014; pp. 403–450, ISBN 9781461469407.
32. Yeh, C.-H. A Problem-based Selection of Multi-attribute Decision-making Methods. *Int. Trans. Oper. Res.* **2002**, *9*, 169–181. [CrossRef]
33. Sang, J.; Bennett, J.C.; Smith, C.H. Estimation of Ballistic Coefficients of Low Altitude Debris Objects from Historical Two Line Elements. *Adv. Space Res.* **2013**, *52*, 117–124. [CrossRef]
34. CelesTrack. Available online: https://celestrak.org/NORAD/elements/gp.php?GROUP=dmc&FORMAT=tle (accessed on 17 November 2023).

35. ESA, "Deimos-1/GEOSAT-1". Available online: https://www.eoportal.org/satellite-missions/deimos-1 (accessed on 17 November 2023).
36. ESA, "UK-DMC-2 (United Kingdom—Disaster Monitoring Constellation-2)". Available online: https://www.eoportal.org/satellite-missions/uk-dmc-2 (accessed on 17 November 2023).
37. ESA, "RISAT-1 (Radar Imaging Satellite-1)". Available online: https://www.eoportal.org/satellite-missions/risat-1 (accessed on 17 November 2023).
38. ESA, "HJ-1 (Huan Jing-1: Environmental Protection & Disaster Monitoring Constellation)". Available online: https://www.eoportal.org/satellite-missions/hj-1 (accessed on 17 November 2023).
39. ESA, "DMC-3 (Disaster Monitoring Constellation-3)". Available online: https://www.eoportal.org/satellite-missions/dmc-3 (accessed on 17 December 2024).

Disclaimer/Publisher's Note: The statements, opinions and data contained in all publications are solely those of the individual author(s) and contributor(s) and not of MDPI and/or the editor(s). MDPI and/or the editor(s) disclaim responsibility for any injury to people or property resulting from any ideas, methods, instructions or products referred to in the content.